

Article

A Residual Middle Triassic Oceanic Island-Seamount in the Maoershan Area, Northwest Tibet: Implications for the Evolution of the Paleo-Tethys Ocean

Chao Li ^{1,2,*}, Junhao Wen ³, Zhongbao Zhao ^{2,4}, Feng Yang ^{1,*}, Jiaxin Yan ⁵, Ye Tian ⁶ and Rong Su ⁷¹ China National Institute of Standardization, Beijing 100191, China² Key Laboratory of Continental Tectonics and Dynamics of Ministry of Natural Resources, Institute of Geology, Chinese Academy of Geological Sciences, Beijing 100037, China³ Administrative and Protection Bureau of China Precambrian Provincial Geological Nature Reserve, Kunming 650600, China⁴ Jiangsu Donghai Continental Deep Hole Crustal Activity National Observation and Research Station, Lianyungang 222300, China⁵ Xi'an Center of Geological Survey, China Geological Survey, Xi'an 710054, China⁶ Beijing Urban Construction Exploration & Surveying Design Research Institute Co., Ltd., Beijing 100101, China⁷ School of Earth Science and Resources, China University of Geosciences, Beijing 100083, China

* Correspondence: lichao0066@163.com (C.L.); yangfeng@cnis.ac.cn (F.Y.)

Abstract: The assemblage of oceanic islands and seamounts, arising from the widespread presence of mature oceans, plays a crucial role in reconstructing the evolutionary history of the paleocean. Oceanic islands or seamounts within the Longmuco-Shuanghu metamorphic complex, a remnant of the Paleo-Tethys Ocean in the central Tibetan Plateau, have seldom been reported due to their remoteness. This study has identified an oceanic island-seamount in the Maoershan area, situated to the west of the Longmuco-Shuanghu metamorphic complex, composed of basalt, diabase, limestone, and siliceous rocks. Based on field observations, petrology, zircon U-Pb dating, whole-rock geochemistry, and Sr-Nd isotopes analyses, we have identified a suite of mafic rocks with OIB affinity. The youngest zircon U-Pb age cluster was concentrated at ~243–241 Ma. The geochemical characteristics of the siliceous rocks indicate a mixture of terrigenous material, suggesting that they formed in a continental margin. In combination with regional geological data, we conclude that the Longmuco-Shuanghu Paleo-Tethys Ocean remained open during the Middle Triassic. Furthermore, a fraction of the oceanic island-seamounts underwent scraping and transformed into a metamorphic complex, while other segments experienced deep subduction, resulting in the formation of high-pressure metamorphic rocks. Collectively, these processes gave rise to the distinctive high-pressure metamorphic complex within the central Qiangtang terrane.

Keywords: central Tibetan Plateau; Longmuco-Shuanghu Paleo-Tethys Ocean; oceanic island and seamount; middle Triassic; in situ origin



Citation: Li, C.; Wen, J.; Zhao, Z.; Yang, F.; Yan, J.; Tian, Y.; Su, R.

A Residual Middle Triassic Oceanic Island-Seamount in the Maoershan Area, Northwest Tibet: Implications for the Evolution of the Paleo-Tethys Ocean. *Minerals* **2023**, *13*, 1551.

<https://doi.org/10.3390/min13121551>

Academic Editor: José Francisco Molina

Received: 22 September 2023

Revised: 12 December 2023

Accepted: 12 December 2023

Published: 15 December 2023



Copyright: © 2023 by the authors. Licensee MDPI, Basel, Switzerland. This article is an open access article distributed under the terms and conditions of the Creative Commons Attribution (CC BY) license (<https://creativecommons.org/licenses/by/4.0/>).

1. Introduction

The ocean plays a crucial role in the Earth's material cycles, landform development, and the evolution of life, making it an essential environment that supports the planet's sustainable development [1,2]. Research on oceanic materials and tectonics is of significant importance for understanding habitable Earth and promoting global sustainable development [3,4].

The oceanic crust and its carriers contain records of the conditions of the ocean at different stages of the Wilson cycle [5]. Particularly during ocean subduction, some fragments of the oceanic crust are scraped off and preserved in the shallow accretionary complex, while the remaining portion and its overlying materials are subducted into the deep crust

and mantle. A part of the subducted materials is exhumed into the complex during later extension [6]. Therefore, the oceanic crust and its overlying materials contain records of ocean subduction and closure, and it is of great significance to study the oceanic remnants to reconstruct the ocean's evolutionary process [7].

The evolution of the Paleo-Tethys Ocean in the Tibetan Plateau is a topic of debate, regarding the presence of an in situ ocean in central Qiangtang, as well as the direction of subduction and the timing of the oceanic closure [8–13]. The Longmuco-Shuanghu complex in the central Qiangtang of the Tibetan Plateau is generally considered to be a remnant of the Paleo-Tethys Ocean [11–14]. In the last three decades, a number of ophiolites, cherts, igneous rocks, and high-pressure metamorphic rocks have been reported within the Longmuco-Shuanghu complex, indicating that the Paleo-Tethys Ocean was open during the Early Paleozoic, expanded rapidly during the Late Devonian–Early Carboniferous, and was reduced after the Late Carboniferous–Early Permian [8,9,15–20]. However, there are few reports on the presence of oceanic islands or seamounts from the Longmuco-Shuanghu metamorphic complex in central Qiangtang [21,22]. The fate of these oceanic islands and seamounts, i.e., whether they were fragmented or subducted to the deep, remains controversial. Moreover, the current youngest reliable Paleo-Tethys oceanic relic in central Qiangtang was recorded in the Maoershan ophiolite, which formed at ~270 Ma, revealing an absence of oceanic material younger than the Early Permian [18]. Therefore, the evolution of the Paleo-Tethys Ocean in central Qiangtang since the Permian, as well as the process and timing of its closure, is still unclear. The search for direct oceanic products within the Longmuco-Shuanghu complex in central Qiangtang has made a significant contribution to our understanding of the evolution of the Paleo-Tethys Ocean.

In this study, we present the results of litho-geochemical analyses, whole-rock Sr-Nd isotopic analyses, and in situ SHRIMP and LA-ICP MS zircon U-Pb dating for the newly discovered oceanic island-seamount located in the Maoershan area of the northwestern part of the Longmuco-Shuanghu complex, within the central Tibetan Plateau. These new findings contribute to the discussion on the origin of the exposed oceanic island-seamount in central Qiangtang and are combined with regional geological constraints to understand the evolution of the Paleo-Tethys Ocean.

2. Geological Setting

The Tibetan Plateau is an amalgamation of terranes that were accreted to the southern margin of Eurasia [10,23]. The interior of the Tibetan Plateau comprises the Kunlun, Songpan-Ganzi, Qiangtang, and Lhasa Terranes from north to south (Figure 1a). The Qiangtang Terrane, situated between Songpan-Ganzi Flysch to the north and Lhasa Terrane to the south, is segregated by two prominent suture zones: the Jinsha Suture to the north and the Bangong-Nujiang Suture to the south [14]. This terrane can be further subdivided into the North Qiangtang and South Qiangtang Terranes by the Longmuco-Shuanghu Suture [13] (Figure 1a).

2.1. Longmuco-Shuanghu Metamorphic Complex

In the central region of the Qiangtang Terrane, a prominent east–west trending complex belt is observed, exposing a series of high-pressure metamorphic rocks and ophiolites [10,16,20] (Figure 1b). These metamorphic rocks primarily comprise garnet phengite schist, marble, eclogite, and blueschist, which were formed via oceanic plate subduction and subsequently exhumed during the Late Triassic period [24–26]. The eclogite and blueschist exhibit geochemical characteristics similar to oceanic island-type basalt or N- and E-MORB-type mafic rocks [15,27–29], suggesting that high-pressure metamorphic rocks are predominantly formed due to oceanic crust subduction with some remnants of continental crust materials. The exposed ophiolites within the complex comprise peridotite, gabbro, basalt, and plagioclase granite, which formed in the following multiple stages as determined by chronology results: 510–430 Ma, 370–340 Ma, and 285–270 Ma [20]. These fragments show N-MORB and SSZ geochemical features [18,30–32]. The Longmuco-

Shuanghu complex encloses Ordovician to Permian continental crustal fragments that exhibit characteristics of a passive continental margin [33]. The aforementioned metamorphic rocks, ophiolites, and continental crust blocks are enveloped by Triassic flysch deposits [34]. The complex overlies extensive Late Paleozoic metasediments by thrusts [35].

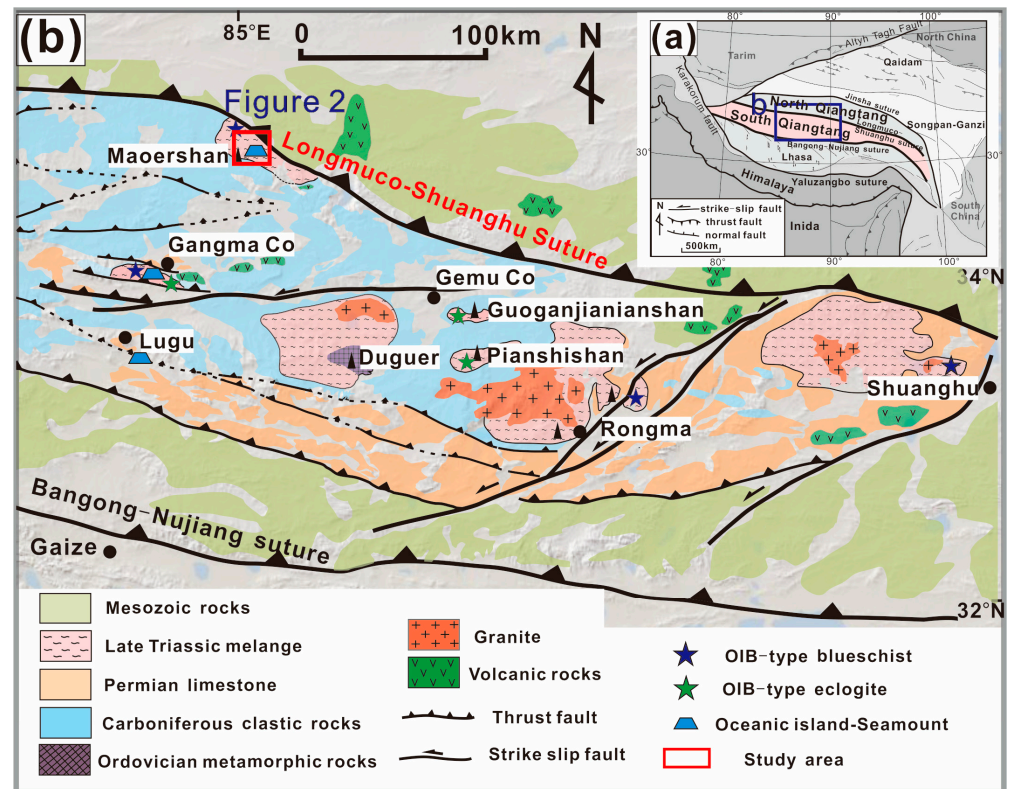


Figure 1. (a) Tectonic framework of the Tibetan Plateau. (b) Regional geological map of the central Qiangtang Terrane of the Tibetan Plateau (modified from [33]). The red box shows the map area in Figure 2.

2.2. Maoershan Complex

The Maoershan complex, exhibiting a typical block-in-matrix structure, has undergone significant multi-stage tectonic events [36] (Figure 2). The blocks that make up the complex, consisting of ophiolite, oceanic island-seamount, amphibolite, and high-pressure granulite, have experienced and thus exhibit variable degrees of deformation and metamorphism [17,18]. These blocks are structurally in contact with others by faults on the outcrop scale, and they are all encompassed by a low-grade metamorphic matrix [36] (Figure 2 and 3).

The study area prominently features mafic-ultramafic rocks, including serpentinized peridotite, metagabbro, metamorphic cumulate gabbro, metabasalt, metadiabase, and a small amount of siliceous rock [18,37]. Based on the zircon U-Pb ages of 274.8 ± 2.7 Ma and 275.2 ± 2.5 Ma in the metagabbro and 280.8 ± 2.2 Ma in the cryptocrystalline vein [18], it was determined that the ophiolite occurred in the Early Permian. The Permian ophiolite exhibits SSZ-type characteristics and was intruded by adakitic granite (271.7 ± 2.3 Ma) [18]. The carboniferous ophiolite exposed on the southern side of the study area consists of pyroxene peridotite, pyroxenite, and cumulate gabbro, which were dated to the Early Carboniferous based on zircon U-Pb ages of 352 ± 3.4 Ma and 351.1 ± 3.9 Ma [18]. Both Carboniferous and Permian ophiolites exhibit positive Sr-Nd isotopes and zircon oxygen isotopes [18]. Silurian high-pressure granulite and amphibolite gneiss have been discovered adjacent to the Carboniferous ophiolite [17] (Figure 2).

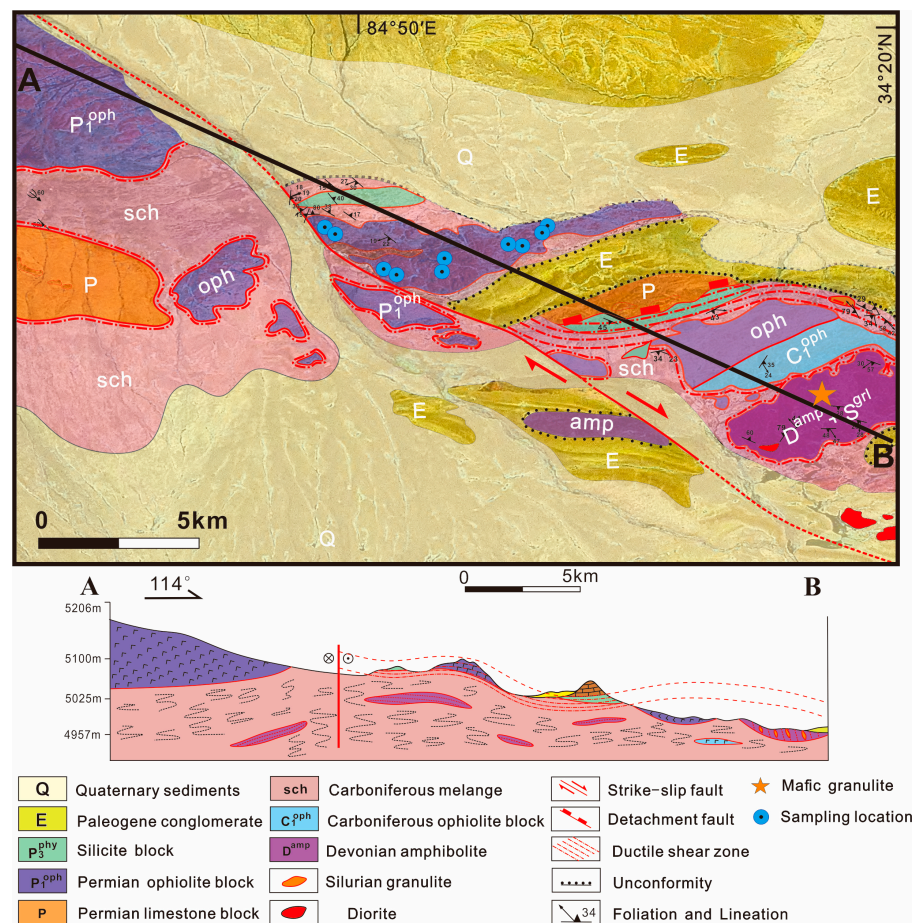


Figure 2. Simplified geological map of the Maershan area in central Qiangtang.

3. Field and Petrographic Observations

In this study, we have identified a specific type of mafic rock that is in conformable contact with siliceous rocks and limestones (Figure 3a–c), which represent remnants of oceanic island and seamount assemblages. These mafic rocks primarily occur in extensive, lenticular formations surrounded by limestone and a clastic matrix (Figure 3a,b). Both the mafic rock and the accompanying limestone and siliceous rocks exhibit foliation, suggesting that they have undergone similar tectonic processes (Figure 3c). Locally, mafic rocks are interbedded with siliceous rocks and limestones in a conformable contact relationship (Figure 3d). The siliceous rocks on both sides of the foliated basalt exhibit a continuous Z-fold, which is indicative of right-lateral shear (Figure 3e). A longitudinal fold is evident, exposing basalt, limestone, and siliceous rocks from the core to the flanks of the fold that exemplify a combination of oceanic crust (Figure 3f).

The mafic rocks primarily consist of plagioclase and pyroxene, with minor occurrences of zoisite (Figure 3g–j). The plagioclase predominantly occurs as subhedral plates, with a typical particle size ranging from 0.2 to 0.8 mm, distributed either directionally or randomly (Figure 3g,h). Single pyroxene crystals, with an average size of 0.2 mm, exhibit subhedral columns or granules and are randomly or interstitially distributed within the plagioclase lattice (Figure 3h,i). Zoisite displays either columnar or granular structures, with an average grain size of approximately 0.2 mm, generally aggregated in subhedral formations while exhibiting disorderly distributions.

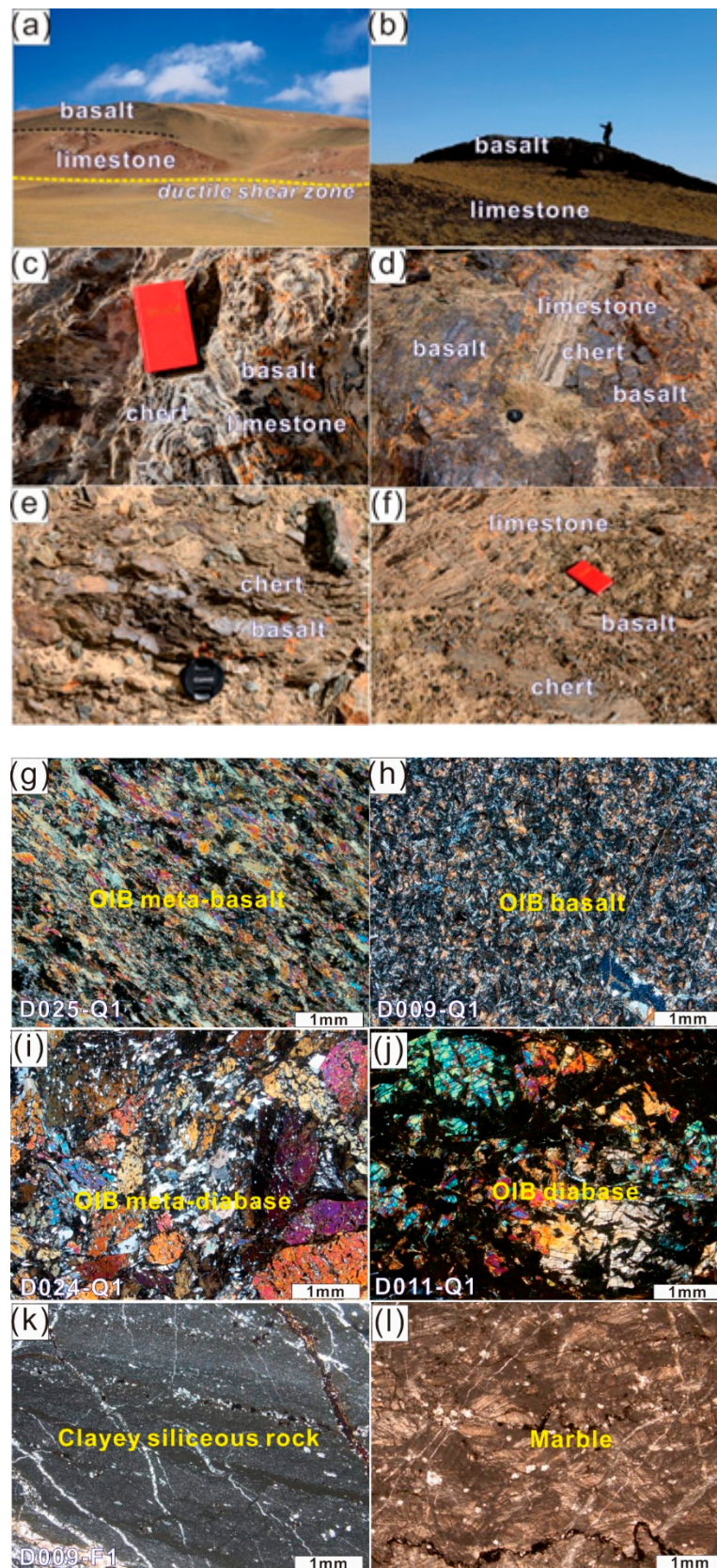


Figure 3. (a–f) Geological outcrops across the ocean island-seamount in the Maoershan area. (g–j) Cross-polarized photomicrographs of mafic rocks. (k,l) Single-polarized photomicrographs of siliceous rocks and marble.

The siliceous rock primarily consists of cryptocrystalline chalcedony mixed with fine clay particles (Figure 3k). The individual grains and their boundaries exhibit indistinct features, displaying either a disordered or slightly directional distribution.

The limestone has largely metamorphosed into marble and is primarily composed of calcite with minor amounts of quartz and muscovite (Figure 3l). The calcite grains exhibit a nearly equiaxed to granular morphology, ranging in size from 0.4 to 1 mm, with a smaller proportion measuring 1–1.6 mm. These grains display a mosaic pattern that is predominantly flat or slightly curved, exhibiting a subtle directional arrangement.

Detailed sample information can be found in the Supplementary Table S1.

4. Analysis Methods

4.1. *In Situ* Zircon U-Pb Geochronology

Zircon grains were separated for U-Pb isotopic analyses using a combination of mechanical crushing, conventional heavy liquid and magnetic techniques, and hand picking under a binocular microscope. Subsequently, representative grains were mounted in epoxy resin and polished. Transmitted and reflected light photomicrographs, along with cathodoluminescence (CL) images, were acquired to help select suitable analytical sites.

U-Pb isotope analyses of zircon were conducted using SHRIMP II at the Beijing SHRIMP Center of Institute of Geology, Chinese Academy of Geological Sciences, and LA-ICP MS at Yanduzhongshi Geological Analysis Laboratories. The instrumental conditions and measurement procedures for SHRIMP were consistent with those described in [38]. The ion beam diameter was set as 25 μm and data were collected in sets of five scans through the masses with 2 nA primary O_2 beams. Standard zircon TEM measurements were performed to calibrate the U, Th, and Pb concentrations and used for isotopic fractionation correction [39]. An LA-ICP MS U-Pb isotope analysis was carried out using a NWR193 laser-ablation microprobe attached to an Analytikjena M90. Isotopic fractionation correction for U-Pb dating was performed using a zircon 91500 external standard. A 30 μm testing denuded diameter was selected. Both the standard samples, 91500 and Plesovice, coincide with the recommended values [40,41]. The trace element contents of zircon were quantified using SRM610 as an external standard and Si as an internal standard [42].

Weighted average age calculations and plots of concordia diagrams for the SHRIMP and LA-ICP MS results were performed in Isoplot/Ex_ver3 (version 3.0, Berkeley Geochronology Center, Berkeley, CA, USA) [43]. The errors of the analyses are quoted at the 1σ level, and common lead adjustment was performed using Andersen method [44]. See Supplementary Tables S2 and S3 for the SHRIMP and LA-ICP MS U-Pb isotopic results.

4.2. Whole-Rock Major and Trace Elements

Whole-rock major and trace element concentrations of eight mafic samples and six chert samples were determined at the Hebei Provincial Institute of Geological and Mineral Survey. Major elements were measured using an Axiosmax X-ray fluorescence spectrometer, with a precision better than 2%. Trace elements were analyzed using an X Series II ICP-MS, with a precision better than 5%. The loss on ignition (LOI) was determined with the gravimetric method. See Supplementary Tables S4 and S5 for a detailed element analysis of the mafic rocks and chert samples, respectively.

4.3. Whole-Rock Sr-Nd Isotopes

Bulk-rock Sr-Nd isotope ratios were determined using a Finnigan Neptune Plus multi-collector ICP-MS at the Institute of Oceanology, Chinese Academy of Sciences (IOCAS). The measurement procedure was adapted from [45]. The measured $^{87}\text{Sr}/^{86}\text{Sr}$ and $^{143}\text{Nd}/^{144}\text{Nd}$ isotope ratios were normalized for the instrumental mass fraction using the exponential law to values of $^{86}\text{Sr}/^{88}\text{Sr} = 0.1194$ and $^{146}\text{Nd}/^{144}\text{Nd} = 0.7219$, respectively. International standards of NBS-987, JNdi-1, and Alfa Hf were employed as bracketing standards to monitor the instrument drift during the analysis of Sr and Nd isotopes. See Supplementary Table S6 for the Sr-Nd isotopic results of mafic rocks.

5. Results

5.1. Zircon U-Pb Geochronology

Representative diabase (D024) and basalt samples (D009) from Maoershan mafic rocks were selected for SHRIMP II and LA-ICP MS U-Pb analyses, respectively (Tables S2 and S3 and Figure 4).

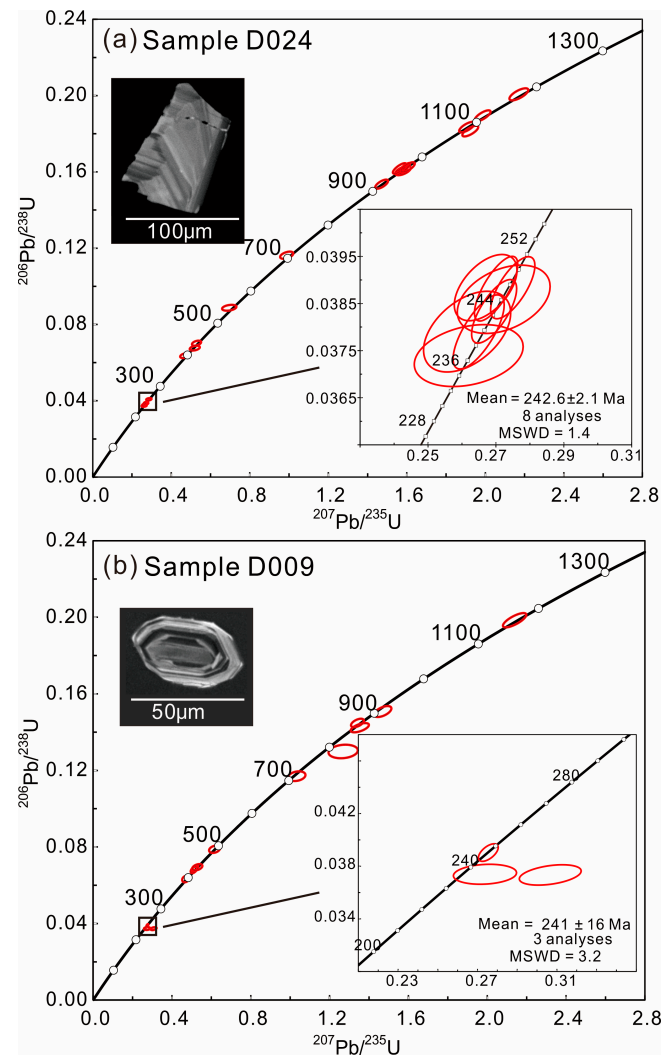


Figure 4. (a) Representative CL image and concordia diagrams showing the results of SHRIMP analyses of zircons from the Maoershan diabase. (b) Representative CL image and concordia diagrams showing the results of LA-ICP MS analyses of zircons from the Maoershan basalt.

The zircon grains from sample D024 are euhedral to subhedral, with an average crystal length of 80 μm and length-to-width ratios ranging from 1.5:1 to 3:1. The cathodoluminescence (CL) images of zircons exhibit a magmatic oscillatory zoning pattern (Figure 4a). The analyzed zircon grains exhibit highly variable U (70–1582 ppm) and Th (36–798 ppm) contents, with Th/U ratios of 0.3–1.6 (Table S2). These characteristics suggest a magmatic origin [46]. The 23 grains from sample D024 yield a diverse age distribution spanning from 240 to 1100 Ma, with the youngest age cluster yielding a weighted mean $^{206}\text{Pb}/^{238}\text{U}$ age of 242.6 ± 2.9 Ma ($n = 8$, mean square weighted deviation (MSWD) = 1.4). Furthermore, fourteen spot analyses on zircons yielded relatively older ages ranging from 1200 to 400 Ma, of which ~960 Ma are relatively concentrated.

The zircons in sample D009 exhibit smaller and more rounded characteristics, with an average crystal length of 50 μm and length-to-width ratios ranging from 1:1 to 2:1 (Figure 4b).

The analyzed zircon grains show highly variable U (58–869 ppm) and Th (70–584 ppm) contents, with Th/U ratios ranging from 0.3 to 1.2 (Table S3). Among the fourteen grains from D009, the youngest three zircon grains were dated at 236.3 ± 3.1 Ma, 236.6 ± 3.1 Ma, and 246.9 ± 2.7 Ma, yielding a mean age of 241 ± 16 Ma ($n = 3$, MSWD = 3.2). Furthermore, another eleven spot analyses yielded older ages ranging from 1200 to 400 Ma, of which ~420 Ma are relatively concentrated.

5.2. Whole-Rock Major and Trace Elements

5.2.1. Mafic Rocks

Major and trace element data of the Maoershan mafic rocks are provided in Table S4. These mafic rocks have undergone calcite alteration and lower greenschist facies metamorphism, resulting in a range of loss-on-ignition values and alterations in the concentrations of mobile elements compared with their original protolith contents. The loss-on-ignition values for these mafic rocks range from 1.39 to 7.49 wt.%, with an average of 4.14 wt.%. The reported weight percentages of major element data as oxides were recalculated to 100%. The concentrations and ratios of immobile elements (e.g., the rare earth elements and high-field-strength elements) and transition metals (e.g., V, Ni, Cr) were not affected by these processes [47] and can be used to classify and determine the samples' petrogenesis and tectonic settings.

The eight samples of Maoershan basalts and diabases exhibit variable SiO₂ contents (45.80–54.50 wt.%, average value of 48.8 wt.%); high contents of TiO₂ (1.9–3.1 wt.%, average value of 2.6 wt.%), Fe₂O₃ (2.4–4.3 wt.%, average value of 3.3 wt.%), FeO (8.7–10.1 wt.%, average value of 9.3 wt.%), MgO (5.4–9.7 wt.%, average value of 7.2 wt.%), CaO (6.8–11.7 wt.%, average value of 9.6 wt.%), and Na₂O (1.7–4.3 wt.%, average value of 2.9 wt.%); low K₂O contents (0.03–1.4 wt.%, average value of 0.51 wt.%); and low Mg[#] values (49.3–62.8, average value of 54.4). The TiO₂ concentrations of Maoershan basalts and diabases (1.9–3.1 wt.%, average value of 2.6 wt.%) are higher compared to typical island arc volcanic rocks (0.58–0.85 wt.%) and mid-ocean ridge basalt (MORB; 1.0–1.5 wt.%), but they are similar to those observed in OIB (2.20 wt.%; [48–50]).

The Maoershan basalt and diabase samples exhibit intermediate total REE concentrations (110.5–205.0 ppm), with slight negative to positive Eu anomalies ($\text{Eu}/\text{Eu}^* = 0.89\text{--}1.38$). These samples exhibit LREE enrichment within the chondrite-normalized REE patterns ($\text{La}_N/\text{Yb}_N = 4.24\text{--}9.19$, $\text{Ce}_N/\text{Yb}_N = 3.41\text{--}7.74$), as well as HFSE enrichment (Nb, Ta, and Ti) (Figure 5a). Trace element concentrations in Maoershan basalts and diabases are slightly lower than those observed in OIB but significantly higher than both E-MORB and N-MORB. These samples exhibit similar patterns regarding the OIB trends in the chondrite-normalized rare element and primitive-mantle-normalized trace element diagrams (Figure 5a,b).

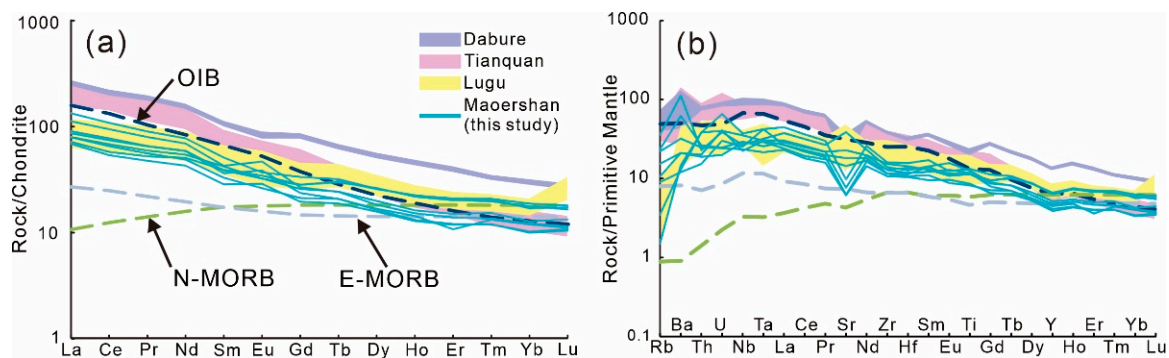


Figure 5. (a) Chondrite-normalized rare earth elements diagram of Maoershan mafic rocks. (b) Primitive-mantle-normalized trace elements diagram of Maoershan mafic rocks. Normalization values of chondrite, primitive mantle, N-MORB, E-MORB, and OIB are from [51]. Data for Dabure and Tianquan oceanic islands are from [21]; data from the Lugu seamount are from [22].

Most of the Maoershan basalt and diabase samples are classified as alkaline basalt on the Zr/TiO_2 vs. Nb/Y immobile element classification diagram (Figure 6), with one sample, D025-1, plotted in the subalkaline basalt area. All samples fall within the intraplate basalt field on the $Ti/100$ vs. Zr vs. $(Y \times 3)$ diagram (Figure 7a), as well as in the ocean island basalt field on the La/Nb vs. La diagram (Figure 7b), indicating that they originated from OIB-type magmas.

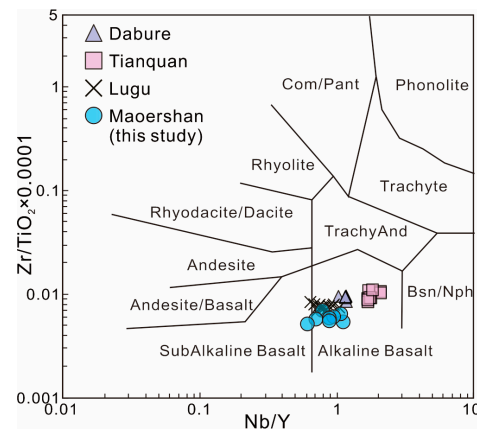


Figure 6. Nb/Y - $Zr/TiO_2 \times 0.0001$ diagram (modified from [48]).

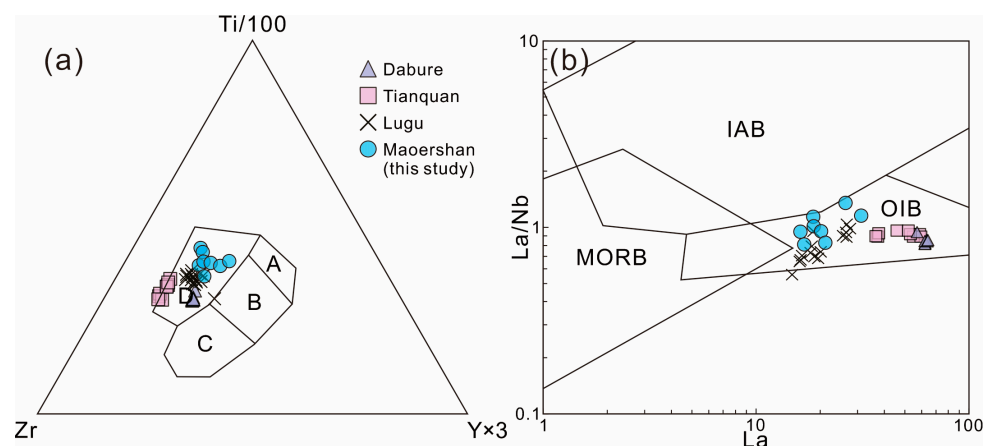


Figure 7. (a) $Ti/100$ - Zr - $Y \times 3$ diagram (modified from [52]); A, island arc tholeiite; B, mid-ocean ridge basalt (MORB) + island arc tholeiite and calc-alkali basalt; C, calc-alkaline basalt; D, intraplate basalt. (b) La/Nb - La diagram (modified from [53]); IAB: island arc basalt.

5.2.2. Cherts

The whole-rock major and trace element data for the Maoershan chert samples are presented in Table S5. These samples exhibit relatively high contents of SiO_2 (73.18–85.04 wt.%), Al_2O_3 (6.09–9.52 wt.%), and Fe_2O_3 (0.80–1.00 wt.%) and low contents of TiO_2 (0.42–0.62 wt.%), MnO (0.06–0.11 wt.%), MgO (1.22–1.92 wt.%), CaO (0.58–3.87 wt.%), Na_2O (2.02–4.16 wt.%), and K_2O (0.29–0.55 wt.%).

The chert samples have relatively high REE contents (567–862.2 ppm). They exhibit flat patterns with slightly negative Eu anomalies and Ce anomalies in the North-American-shale-normalized REE diagram (Figure 8a) and exhibit LREE enrichment with slightly negative Eu anomalies in the chondrite-normalized REE diagram (Figure 8b), which closely resemble those observed in a continental margin setting [54].

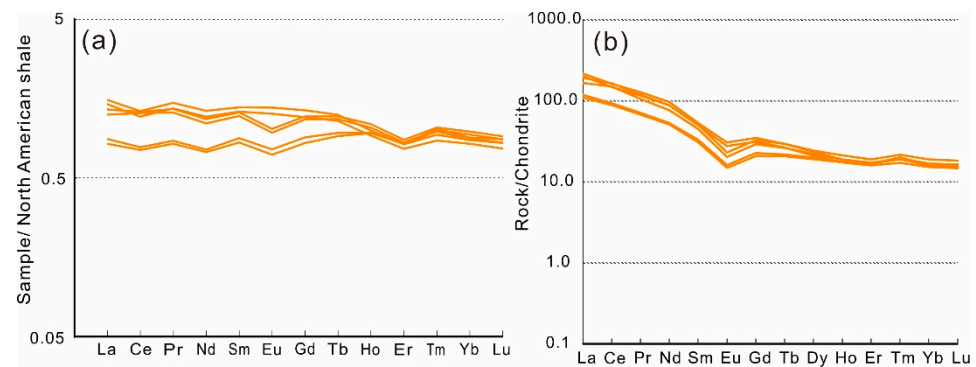


Figure 8. (a) NASC- and (b) chondrite-normalized REE patterns of Maoershan siliceous rocks (normalization values of North American shale are from [55]; normalization values of chondrite are from [51]).

5.3. Whole-Rock Sr-Nd Isotopes

Four representative mafic samples were analyzed to determine their Sr and Nd isotope compositions (Table S6 and Figure 9). Maoershan basalts have variable Sr-Nd isotopic compositions, with have initial $^{87}\text{Sr}/^{86}\text{Sr}$ ratios of 0.703720–0.706373 and initial $^{143}\text{Nd}/^{144}\text{Nd}$ ratios of 0.512324–0.512659, and they possess relatively positive $\epsilon\text{Nd}(t)$ values within the range of 0–6.5. The wide variety of initial $^{87}\text{Sr}/^{86}\text{Sr}$ ratios may reflect seawater alterations due to the more mobile geochemical properties of Sr compared to Nd [56]. In the $^{87}\text{Sr}/^{86}\text{Sr}$ versus $\epsilon\text{Nd}(t)$ diagram, the samples are correlated with OIB, and trend towards enriched mantle II (EMII) end-members [57], which is consistent with a previous study of the Lugu seamount [22] (Figure 9).

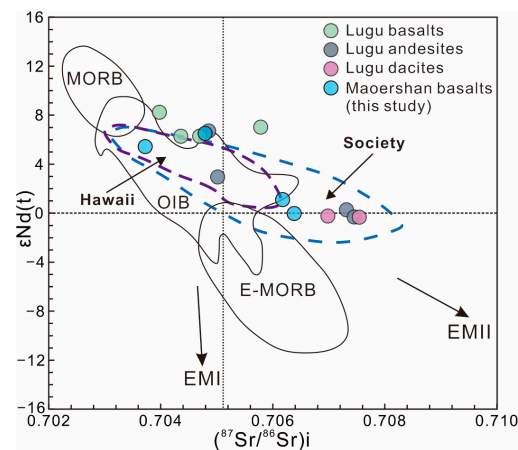


Figure 9. $(^{87}\text{Sr}/^{86}\text{Sr})_i$ -Nd(t) diagram of Maoershan mafic rocks (modified from [58]). DM—depleted mantle, PM—primitive mantle, EM—enriched mantle, MORB—mid-ocean ridge basalt, OIB—oceanic island basalt. Hawaii and Society data are from [59]; Lugu lavas data are from [22].

6. Discussion

6.1. Age of Maoershan Oceanic Island-Seamount

Determining the age of formation for the Maoershan oceanic island-seamount is crucial for understanding the evolution of the Longmuco-Shuanghu Paleo-Tethys Ocean. Therefore, we conducted in situ zircon U-Pb dating on two representative mafic rocks from the Maoershan oceanic island-seamount. Our analysis revealed similar characteristics in both mafic samples, with a cluster of youngest zircon dating at ~240 Ma and relatively older zircons ranging from 400 Ma to 1200 Ma (Figure 4). Furthermore, we discuss the origin and significance of different zircon ages to ascertain the formation age of Maoershan oceanic island-seamount.

It has been found that early recycled zircons can also be well preserved in mantle magmas, probably due to low Pb^{2+} diffusion and the presence of mantle minerals such as olivine and pyroxene, which act as seals for these early-formed zircons [60,61]. This phenomenon has also been documented in various geological settings, including oceanic island-seamounts, oceanic plateau, abyssal plain, and even mid-ocean ridge within the modern Atlantic and Indian oceans [61–63]. Therefore, we propose that the older zircons ranging from 400 Ma to 1200 Ma in the mafic rocks of the Maoershan oceanic island-seamount are likely to be the recycled zircons. The upwelling hot mafic mantle magma scavenges xenoliths and later disaggregates them, releasing zircon xenocrysts, thereby leading to the incorporation of zircon xenocrysts into mafic magma [64]. This process is supported by the OIB affinity exhibited by the Maoershan mafic rocks without obvious contamination (6.2).

Previous studies have demonstrated that the youngest zircon peak with oscillatory zoning can represent the age of final crystallization and formation of magma [60]. Zircon grains from the youngest zircon peak in Maoershan mafic rocks exhibit distinct oscillating rings, along with the idiomorphic morphology and Th/U ratios > 0.1 (Figure 4). Hence, we propose that the two youngest zircon peaks represent the formation age of Maoershan mafic rocks. Taking into account the two youngest age peaks from diabase and basalt (~241 Ma, ~243 Ma), we conclude that the Maoershan oceanic island-seamount formed during the Middle Triassic period.

6.2. Petrogenesis of Maoershan OIB-Like Mafic Rocks

6.2.1. Crustal Contamination

It is crucial to discern the presence of crustal contamination when discussing the petrogenesis and magmatic source of mafic rocks. The rapid rise in Th and Ta ratio can serve as a reliable indication of crustal contamination [65]. The Maoershan basalts and diabases have relatively low Th values (1.32–3.32 ppm, with a mean value of 2.07 ppm) and small variations in Th/Ta ratios (0.75–2.63, with a mean value of 1.75), which are similar to those in volcanic rocks derived from primitive mantle (Th/Ta = 2.3; [65]) and significantly lower than those in the upper crust (Th/Ta > 10). In addition, there is no positive correlation between SiO_2 and Th/Ta ratios (Figure 10a), indicating that the mafic rocks have not undergone any crustal contamination. Incompatible element ratios tend to remain constant during the fractional crystallization process but shift considerably during magma mixing or crustal contamination. The Maoershan basalts and diabases also have small variations in Zr/Nb, Th/Nb, and La/Sm ratios (6.74–8.15, 0.07–0.13, and 2.85–4.07, respectively), and there is no obvious correlation between SiO_2 and Zr/Nb, Th/Nb, and La/Sm ratios (Figure 10b–d), which is consistent with those mafic rocks that are not affected by crustal contamination. This conclusion is also demonstrated in the $(La/Nb)_{PM}-(Th/Nb)_{PM}$ diagram; most of the samples are located in the oceanic basalt region, with no crustal contamination trend (Figure 11a).

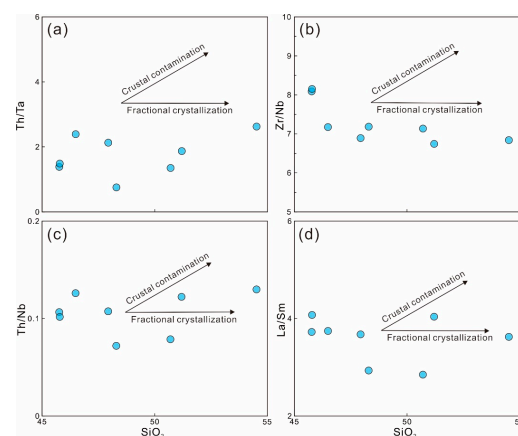


Figure 10. Plots of Th/Ta, Zr/Nb, Th/Nb, La/Sm vs. SiO_2 diagrams of Maoershan mafic rocks. (a) Th/Ta– SiO_2 diagram; (b) Zr/Nb– SiO_2 diagram; (c) Th/Nb– SiO_2 diagram; (d) La/Sm– SiO_2 diagram.

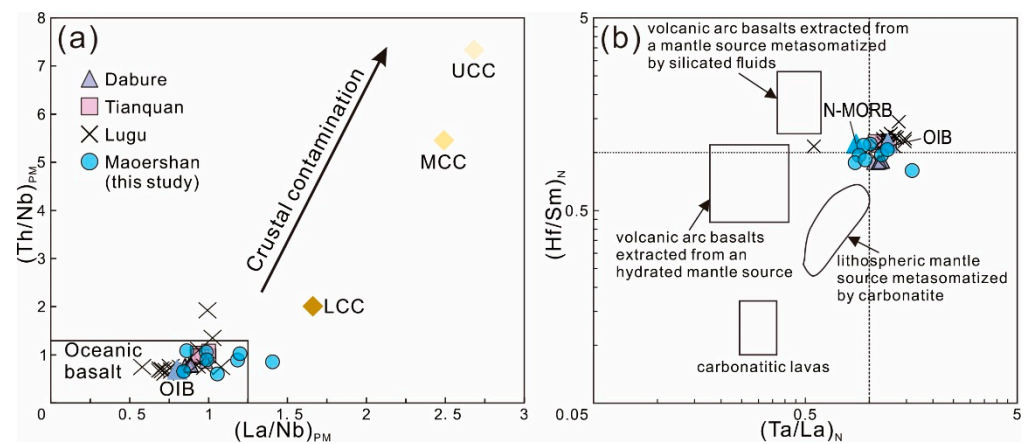


Figure 11. (a) $(\text{La}/\text{Nb})_{\text{PM}}-(\text{Th}/\text{Nb})_{\text{PM}}$ diagram, modified from [66]; UCC, MCC, and LCC values are from [67], OIB and N-MORB values are from [51]. (b) $(\text{Ta}/\text{La})_{\text{N}}-(\text{Hf}/\text{Sm})_{\text{N}}$ diagram, modified from [68]; OIB, N-MORB, and PM values are from [51], DM values are from [69].

The Longmuco-Shuanghu Paleo-Tethys Ocean underwent subduction and closure as a back-arc oceanic basin during $\sim 270\text{--}230$ Ma [18,20], indicating the complexity of ocean declination. Thus, after ruling out continental crust material contamination, it was essential to ascertain whether the magma is contaminated by the subduction oceanic crust. Island arc basalts (IABs) produced by the oceanic crust subduction typically have a $[\text{Nb}/\text{Th}]_{\text{PM}} \ll 1$ and a $[\text{Ta}/\text{U}]_{\text{PM}} \ll 1$, while MORB and OIB exhibit a $[\text{Nb}/\text{Th}]_{\text{PM}} \geq 1$ and a $[\text{Ta}/\text{U}]_{\text{PM}} \geq 1$ [70]. The Maoershan basaltic rocks have a $[\text{Nb}/\text{Th}]_{\text{PM}}$ between 0.92 and 1.66 (with a mean ratio of 1.19) and $[\text{Ta}/\text{U}]_{\text{PM}}$ values between 0.65 and 1.45 (with a mean ratio of 0.97), suggesting that the Maoershan basaltic rocks are not contaminated by the subduction oceanic crust. This is also demonstrated in the $(\text{Ta}/\text{La})_{\text{N}}-(\text{Hf}/\text{Sm})_{\text{N}}$ diagram, where the samples fall within the OIB area (Figure 11b), far away from the region where the mantle source is influenced by metasomatism.

Furthermore, the Maoershan basaltic rocks have high contents of Nb (16.3–27.0 ppm, with an average of 20.7 ppm), Ta (0.90–1.77 ppm, with an average of 1.32 ppm), and Ti (11325–18598 ppm, with an average of 15336 ppm) and high Ti/Y ratios (510–850, with an average of 645). These characteristics are indicative of high-Nb volcanic rock [71] and high-Ti basalt [72], thereby effectively excluding the possibility of crustal contamination, as they exhibit no apparent depletion in Nb, Ta, and Ti, which are commonly observed in both continental crust and recycled oceanic crust [67,70]. The process of continental or oceanic crustal contamination can result in the manifestation of apparent continental crust or island arc signatures, but these phenomena have not been observed in Maoershan basaltic rocks.

6.2.2. Magma Source

The mafic rocks of oceanic island-seamount are very complex, including different types of basalts, such as tholeiite and alkaline series [73,74]. The broad compositional diversity of basaltic magmas may originate from a single parental magma, with variations in composition being controlled by pressure or the associated oceanic lithospheric thickness [75,76]. Although one mafic sample is plotted in the subalkaline basalt area, which differs from other samples (Figure 6), we believe that all mafic samples arise from the same parental magma, based on our field observation and geochemical characteristics (Figures 3, 5 and 7). Therefore, we consider these mafic samples as the same magmatic series to discuss the magma source.

Basaltic magma is generally derived from the partial melting of mantle peridotite, and garnet and spinel have a primary influence on the REEs in the magma, rather than olivine, clinopyroxene, and orthopyroxene [77,78]. Basalts derived from garnet lherzolite exhibit obvious fractionation between the LREEs and HREEs, while the basalts derived from spinel lherzolite exhibit inconspicuous fractionation between the LREEs and HREEs [79,80].

Yb is compatible with garnet, whereas Sm is incompatible. Consequently, during the partial melting of garnet peridotite, a lower degree of melting results in more pronounced differentiation between Yb and Sm. In contrast, the partial melting of spinel peridotite does not affect the constant Sm/Yb ratio.

The Maoershan basalts and diabases exhibit high La_N/Yb_N and Ce_N/Yb_N ratios, as well as chondrite-normalized REE patterns that are enriched in LREEs (Figure 5a), suggesting that the Maoershan basaltic rocks are derived from garnet peridotite. Partial melting (approximately 5–10%) of a hypothetical mantle source containing spinel + garnet lherzolite (50:50) would produce REE concentrations similar to those in the Maoershan basalts and basaltic diabases in the Sm/Yb vs. Sm diagram (Figure 12a).

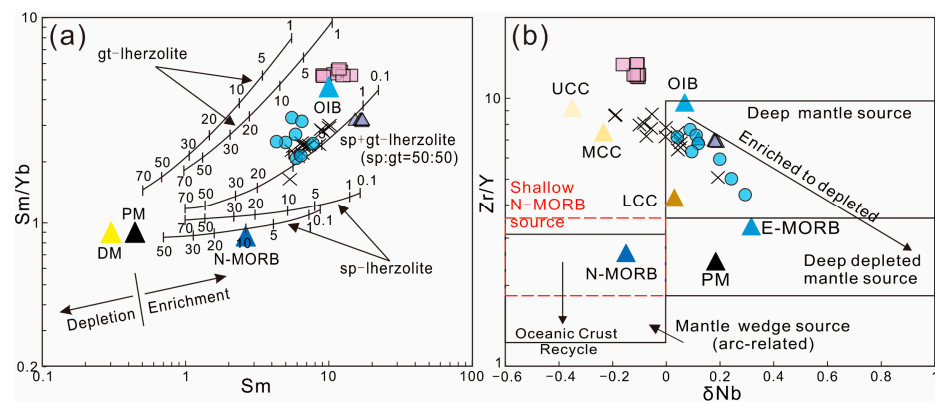


Figure 12. (a) Sm/Yb–Sm diagram (modified from [81]); N-MORB, OIB, and PM values are from [51], the DM (depleted MORB mantle) is from the compilation of [82]. (b) Zr/Y– δNb diagram (modified from [83]); N-MORB, OIB, E-MORB, and PM values are from [51], UCC, MCC, and LCC values are from [67].

Zr/Y ratios and δNb values can provide valuable information on the basalts' magma source, and high Zr/Y ratios and positive δNb values indicate a potential deep-mantle source for the OIB-like rocks [83]. The Maoershan basaltic rocks are located in the deep enriched mantle source region and exhibit a trend from highly enriched to moderately enriched in the Zr/Y– δNb diagram (Figure 12b).

The Sr-Nd isotopes of the Maoershan basaltic rocks are similar to those of Lugu oceanic island lavas [22], exhibiting an EMII-type enrichment trend (Figure 9) and implying that the Maoershan basaltic rocks originated from a mantle source similar to that of modern Hawaii and Society magmas [59]. The scattered Sr-Nd isotopes may reflect the heterogeneity of the magma sources [22].

6.2.3. Fractional Crystallization

The La/Sm ratios remained constant as the La content increased, indicating that the Maoershan basaltic magma underwent fractionation rather than partial melting (Figure 13a). There is an obvious negative correlation between MgO and SiO₂, combined with Ni content increases along a convex upwards curve with Cr, indicating olivine fractionation (Figure 13b,c). The constant Eu* values observed with increasing MgO contents suggest minimal plagioclase fractionation (Figure 13d). Most Cr and Ni concentrations and Mg[#] values in the Maoershan basaltic rocks (Cr = 101–331 ppm, Ni = 62–197 ppm, Mg[#] = 49–63) exhibit lower values compared to those observed in primary-mantle-derived magmas (Cr = 300–500 ppm, Ni = 300–400 ppm, Mg[#] = 68–75; [84,85]). These correlations indicate that the Maoershan basaltic magma underwent fractional crystallization of olivine, chromite, and pyroxene [86,87].

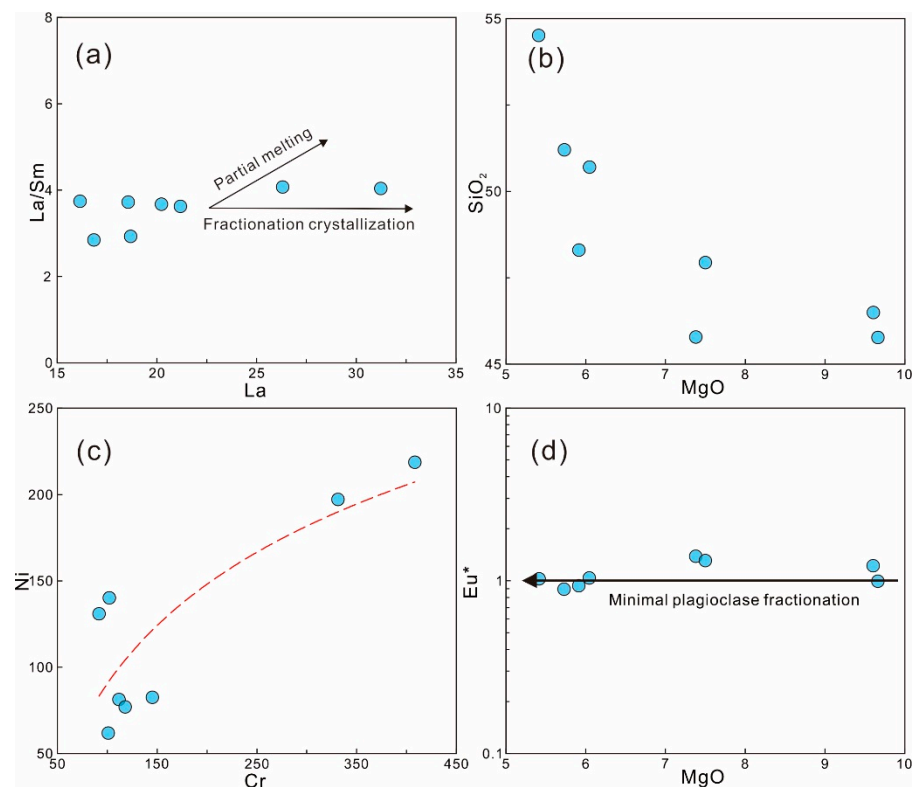


Figure 13. Plots of La/Sm, SiO₂, Eu* vs. MgO and Ni vs. Cr diagrams of the Maershan mafic rocks. (a) La/Sm–La diagram; (b) SiO₂–MgO diagram; (c) Ni–Cr diagram; (d) Eu*–MgO diagram.

The above evidence shows that the Maershan basaltic rocks are OIB-type basaltic rocks, which originated from low-degree partial melting of spinel–garnet lherzolite in the mantle, indicating a deep enriched mantle plume origin. Partial melting occurs at the top of the low-velocity seismic wave zone (LVZ) and at the base of the oceanic lithosphere [76,88], where it exhibits a transition phase from garnet to spinel. The ascending Maershan basaltic magmas underwent varying degrees of fractional crystallization without being contaminated by the crust.

6.3. Tectonic Environment

6.3.1. Mafic Rocks

The conformable contact between the mafic rocks, siliceous rocks, and limestone and the recurring sequence of basalt–chert–limestone indicate a typical oceanic island–seamount exposed in the complex. Geochemical analyses of the Maershan basaltic rocks, exhibiting OIB-like features, and the lack of contamination with terrestrial sediments indicate varying degrees of fractional crystallization, further demonstrating that the Maershan basaltic rock is a typical Middle Triassic oceanic island and seamount formed by the eruption of a deep enriched mantle plume in the basin of the Longmuco–Shuanghu Paleo-Tethys Ocean, similar to the Tianquan, Dabure, and Lugu oceanic islands and seamounts [21,22].

6.3.2. Cherts

Cherts, characterized by a chemical inertness and an exceptional resistance to weathering and alteration, exhibit relatively simple and stable elemental compositions. These compositions reflect constituents such as volcanic detritus, terrigenous clasts, and hydrothermal precipitates [89], making cherts valuable indicators of provenance due to their unique geochemical properties. The geochemical characteristics exhibited by cherts provide valuable insights into the tectonic setting and depositional environment [54]. Three primary depositional regimes, spreading ridge proximal, ocean basin floor, and continental margin,

have been identified [90]. The continental margin regime encompasses back-arc basins, marginal seas, epicontinental seas, and open continental shelves [54].

The cherts exhibit conformable contact with the Maoershan OIB-type mafic rocks (Figure 3), and an analysis of their geochemistry could further enhance our comprehension of the oceanic island-seamount's tectonic setting. The Al/(Al + Fe + Mn) ratios of the samples range from 0.62 to 0.68, closely aligning with biogenic cherts (0.6), as supported by the Al-Fe-Mn triangulation diagram (Figure 14a). The North-American-shale-normalized REE patterns exhibit a rightward inclination (Figure 8b), further supporting a non-hydrothermal sedimentary chert origin. Additionally, the U/Th ratios of the samples range from 0.16 to 0.27, which is inconsistent with hydrothermal deposition.

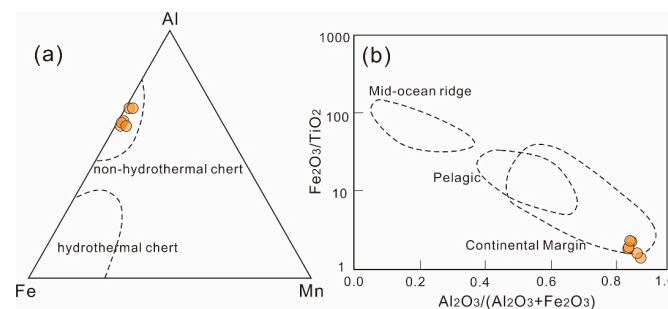


Figure 14. Geochemical data of cherts plotted on the (a) Al vs. Fe vs. Mn and (b) Fe₂O₃/TiO₂ vs. Al₂O₃/(Al₂O₃ + Fe₂O₃) diagrams (modified from [90,91]).

The cherts have high Al₂O₃ contents (6.09–9.52 wt.%), indicating a large contribution from terrigenous material during their deposition. The MnO/TiO₂ ratios, ranging from 0.13 to 0.18, suggest that the samples were located in continental slopes and marginal sea deposits in close proximity to land. The Al₂O₃/(Al₂O₃ + Fe₂O₃) ratios, ranging between 0.88 and 0.92, significantly deviate from those observed in the mid-ocean ridge (<0.4) and oceanic basin (0.4–0.7), suggesting their proximity to the continental margin. The (La/Ce)_{shale} ratios range from 0.98 to 1.19 and δCe_{shale} ranges from 0.78 to 1.32, suggesting that the cherts were formed in a continental margin setting. Moreover, the V/Y ratios, ranging from 1.09 to 1.76, exhibit similarities to siliceous rocks found in continental margins. These findings are also supported by the Fe₂O₃/TiO₂-Al₂O₃/(Al₂O₃ + Fe₂O₃) diagram (Figure 14b).

In summary, the field occurrence and geochemistry evidence strongly indicate that the Maoershan basaltic rocks and cherts are from a typical oceanic island-seamount that formed in the narrow oceanic basin of the Longmuco-Shuanghu Paleo-Tethys Ocean, resembling a residual Mediterranean-type basin [92].

6.4. An Ocean Island-Seamount Chain of ~240 Ma in the West Segment of the Longmuco-Shuanghu Paleo-Tethys Ocean

Recently, a series of Permian–Triassic mafic rocks have been reported in the Longmuco-Shuanghu metamorphic complex, but they are thought to have been formed in different tectonic settings, including oceanic islands and mafic dyke swarms formed during the passive margin extension or upwelling of asthenosphere [6,21,22,93]. To the east, the Rongma area contains mafic dykes dated at ~230–237 Ma, which contain gabbros characterized by high Ti and Nb contents, as well as LREE enrichments. It has been speculated that they are associated with the mantle wedge during the subduction of oceanic ridges into trenches [6]. To the west, the mafic dykes widely exposed in the Duguer area at ~239 Ma are thought to have formed during regional extension associated with the passive margin, and it is speculated that the residual ocean could potentially have spanned a distance of around 200 km [93]. However, there is increasing evidence that the contemporaneous mafic rocks came from ocean island-seamounts [21,22]. The blueschists and eclogites with OIB characteristics formed at ~238 Ma, suggesting that their origins

are linked to the subduction of oceanic island-seamounts [26]. But where are the oceanic island-seamounts that have not undergone high-pressure metamorphism?

Low-grade metamorphic mafic rocks with OIB characteristics in the Longmuco-Shuanghu complex have been reported in the Gangma Co and Lugu areas. Dabure and Tianquan OIB-type mafic rocks aged between ~250 and 241 Ma, along with siliceous rocks formed in the continental margin, have been identified in the Gangma Co area, the southern part of the Longmuco-Shuanghu complex [21]. Further south of Dabure, Lugu OIB-type mafic rocks and lavas aged ~229 Ma have been detected [22]. The above three oceanic island-seamounts indicate the presence of an Early–Late Triassic oceanic island-seamounts in the central and southern part of the Longmuco-Shuanghu complex (Figures 5–7). The Maoershan oceanic island-seamount in the northwest part of the Longmuco-Shuanghu complex has been studied in this paper. The Maoershan oceanic island-seamount is located in a narrow ocean basin, which is evidenced by the presence of mafic magma that was not contaminated by terrestrial sediments during volcanic eruptions, but the siliceous rocks indicate a mixture of terrigenous material. The oceanic island/seamount's mafic magma source has been demonstrated to exclusively originate from deep mantle plumes or hotspots [76]. Therefore, we propose that despite the Paleo-Tethys Ocean being a narrow ocean basin around 240 Ma, mantle hotspots were still widely distributed within it. Collectively, the Maoershan, Gangma Co, and Lugu oceanic island-seamounts imply the presence of an oceanic island-seamount chain within the Paleo-Tethys Ocean around 240 Ma.

6.5. Significance in the Evolution of the Longmuco-Shuanghu Paleo-Tethys Ocean

6.5.1. Closure Timing of the Longmuco-Shuanghu Paleo-Tethys Ocean

The origin of the Longmuco-Shuanghu complex has remained a subject of ongoing controversy, regarding whether it represents an outcome of an in situ evolution within the Paleo-Tethys Ocean [10–12,14]. The presence of the Longmuco-Shuanghu oceanic island-seamount chain, including the Dabure oceanic island, Tianquan oceanic island and Lugu seamount, and recently identified Maoershan ocean island-seamount, indicates the existence of a certain-sized ocean basin between the southern and northern Qiangtang terranes at ~240 Ma. Additionally, the presence of low-temperature and high-pressure metamorphic rocks such as Gangma Co and Lanling blueschists implies the cold subduction of oceanic crust [16]. The distinct geochemical characteristics of the cherts and basalts within the Longmuco-Shuanghu complex, along with their clear differentiation from those within the Jinsha suture [11], collectively support that this complex is a product of in situ oceanic subduction, rather than the exposure of a remotely transported metamorphic core complex during southward subduction of the Jinsha complex, which was subsequently exhumed by a domal structure [10,23].

The closure times of the Paleo-Tethys Ocean have been another subject of considerable debate. While some studies suggest that the closure was no later than the Late Triassic, possibly in the Early or Middle Triassic [94,95], alternative viewpoints suggest a subduction state persisting until the Middle Triassic, finally closing in the Late Triassic [16,30,32]. The slab break-off occurred prior to the Middle Triassic, implying that the closure might have taken place in the Early Triassic or Late Permian [96]. The above arguments lead to a broad range of proposed closure timings for the western segment of the Paleo-Tethys Ocean, spanning from the Late Permian to the Early or Late Triassic. Moreover, previous studies have suggested temporal differences in the closure of the ocean between its eastern and western segments based on limited data [21,97].

The existence of an oceanic island-seamount chain in the Longmuco-Shuanghu complex at ~240 Ma, combined with the coeval island arc and the Triassic Tianquanshan flysch deposits [98], implies that the western segment of the Paleo-Tethys Ocean remained unclosed at 240 Ma. High-pressure metamorphic rocks in central Qiangtang were exhumed during the middle Late Triassic (~220 Ma; [30]), with an unconformity developing prior to the middle–late Late Triassic Wanghuling Formation [99]. The above evidence indicates that the western segment collided at 220–210 Ma. On the east segment, northward sub-

duction of the Paleo-Tethys Ocean continued at ~221 Ma [97], evidenced by the Baqing eclogite formed during the Early–Late Triassic (227–221 Ma; [100]). Consequently, the timing difference in the oceanic closure between east and west is insignificant (<20 Ma), and the complete closure of the Paleo-Tethys Ocean likely occurred around ~220–210 Ma in the central Tibetan Plateau.

6.5.2. The Evolution Process of the Longmuco-Shuanghu Paleo-Tethys Ocean during the Permian–Triassic Period

Based on findings from prior research on ophiolites, igneous rocks, and metamorphic rocks, this study provides insights into the evolutionary history of the Longmuco-Shuanghu Paleo-Tethys Ocean since the Permian.

The Paleo-Tethys Ocean underwent arc-related subduction from ~285 to 270 Ma. The ophiolites that were scraped off during this process are predominantly located in the Gemu Co and Maoershan areas, comprising serpentized peridotites, cumulate gabbros, diorites, and siliceous sedimentary rocks [18]. The Gemu Co ophiolites exhibit SSZ-type geochemical characteristics, while the Maoershan ophiolites show features of both N-MORB and IAB, supporting that they were formed in a back-arc basin [18,101].

In the subsequent period of 250–240 Ma, a series of oceanic island-seamounts emerged along the western flank of the Paleo-Tethys Ocean as a result of mantle hotspot activity (Figure 15a). The oceanic island-seamounts found in the Gangma Co, Maoershan, and Lugu areas were formed at ~250–241 Ma, ~240 Ma, and ~229 Ma, respectively, suggesting the presence of continuous volcanic activity during 250–230 Ma [21,22]. Simultaneously, these mantle hotspots likely intruded into the passive continental margin in southern Qiangtang, resulting in the formation of the 239 Ma mafic dykes in the Duguer area [93]. Several oceanic islands and seamounts have experienced northward subduction during the period of 240–220 Ma, resulting in the formation of Hongjishan, Gangma Co, Pianshishan, and Guoganjianian complexes in the central Qiangtang area [20]. These complexes are characterized by the OIB-affinity eclogites and blueschists with protolith ages of ~240 Ma [15,26,29]. However, due to density differences, most eclogites and blueschists underwent deep subduction into the lower crust and mantle and were not uplifted to the surface [102]. Meanwhile, some oceanic island-seamounts were scraped off from the oceanic crust as a whole and incorporated into the complex [29] (Figure 15b).

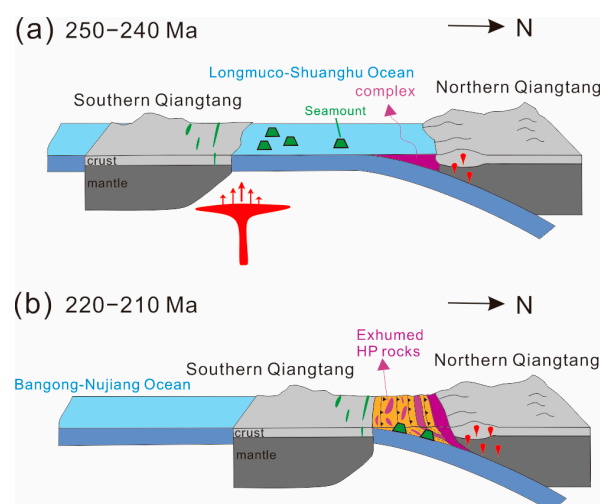


Figure 15. Schematic model showing the late Permian–Triassic evolution of the Longmuco-Shuanghu Paleo-Tethys Ocean (modified from [20,103]). (a) Subduction of the Paleo-Tethys Ocean and emergence of the oceanic island-seamounts in the ocean; (b) Closure of the Paleo-Tethys Ocean and final formation of the metamorphic complex, with the exhumation of the high-pressure rocks into the complex.

The Paleo-Tethys Ocean continued to undergo northward subduction after ~240 Ma, leading to the formation of mafic volcanic rocks in northern Qiangtang at 237–235 Ma [104] and granite at approximately 230 Ma [105]. The eastern segment of the Paleo-Tethys Ocean also experienced a surge of subduction-related magmatic activity from 250 to 230 Ma, as evidenced by the Nb-enriched basalt and adakitic rocks at 229 Ma [106] and the subduction-related rhyolites at 247–241 Ma [107] in eastern Tibet, indicating that the ocean had not yet closed.

Following the collision between the northern and southern Qiangtang terranes during the 220–210 Ma period, the subducted plates broken off, leading to an extensional environment that caused a large-scale exhumation of OIB-affinity eclogites and blueschists in central Qiangtang [29]. The Nadigangri bimodal volcanic rocks in the Qiangtang terrane, indicative of intracontinental rift settings and dated at 220–215 Ma, mark the complete closure of the ocean [108,109]. Widespread magmatic activity in central Qiangtang at 220–210 Ma also signals a transition from subduction to an extensional environment following the collision [110]. The overlying materials on the oceanic lithospheric slices, such as oceanic island-seamount and ophiolites, which were scraped off at shallow depths, along with the exhumated high-pressure metamorphic rocks, were incorporated within the matrix of oceanic sediment matrix [13]. Eventually, they contributed to the formation of a large-scale complex characterized by high-pressure metamorphic rocks in central Qiangtang [35] (Figure 15b).

7. Conclusions

(1) An assemblage of oceanic island-seamount has been identified in the Maoershan area, located northwest of the Longmuco-Shuanghu complex. The Maoershan oceanic island-seamount primarily consists of basalt, diabase, limestone, and siliceous rocks. These rocks have experienced significant deformation associated with subduction.

(2) The Maoershan oceanic island-seamount was formed during ~243–241 Ma, as evidenced by zircon U-Pb dating of the mafic rocks. These mafic rocks primarily originated from enriched mantle plume material, resulting in geochemical characteristics that align with the properties of ocean island basalts (OIBs).

(3) The Maoershan cherts contain terrigenous material, indicating their deposition along a continental margin. This suggests that the Paleo-Tethys Ocean had already transitioned into a confined ocean basin.

(4) The northwestern segment of the Paleo-Tethys Ocean did not close during the Middle Triassic period. A series of oceanic island-seamounts were present around ~240 Ma, potentially associated with mantle hotspot activity. Some of these oceanic island-seamounts experienced deep subduction, leading to the formation of high-pressure metamorphic rocks. In contrast, others were directly accreted into the accretionary wedge, thereby contributing to the development of the Longmuco-Shuanghu metamorphic complex.

Supplementary Materials: The following supporting information can be downloaded at: <https://www.mdpi.com/article/10.3390/min13121551/s1>, Table S1: Maoershan sample information; Table S2: Maoershan mafic rock SHRIMP Zircon U-Pb contents; Table S3: Maoershan mafic rock LA-ICP MS Zircon U-Pb contents; Table S4: Maoershan mafic rock major element (%) and trace element (ppm); Table S5: Maoershan chert major element (%) and trace element (ppm); Table S6: Maoershan mafic rock Sr-Nd isotopic compositions.

Author Contributions: C.L. contributed to the conception of the study and wrote the original draft; J.W. performed the data analyses and wrote the manuscript; Y.T. and R.S. contributed significantly to field geological work; Z.Z., F.Y. and J.Y. helped perform the analysis with constructive discussions. All authors have read and agreed to the published version of the manuscript.

Funding: This work was funded by the National Key Research and Development Program of China (2022YFC3802901), the Natural Science Foundation of China (42202257, 4190020921), the Special Funds of the National Natural Science Foundation of China (41941016-3), the Second Tibetan Plateau Scientific Expedition and Research Program (STEP) Grant (2019QZKK0901), the Key Special Project for Introduced Talents Team of Southern Marine Science and Engineering Guangdong Laboratory (Guangzhou) (GML2019ZD0201).

Data Availability Statement: All data used in this study are freely available.

Acknowledgments: We express our thanks to anonymous reviewers for their constructive comments, which significantly improved the manuscript.

Conflicts of Interest: Author Ye Tian was employed by the company Beijing Urban Construction Exploration & Surveying Design Research Institute Co., Ltd. The remaining authors declare that the research was conducted in the absence of any commercial or financial relationships that could be construed as a potential conflict of interest.

References

1. Kennedy, D. *Science* **2005**, *309*, 19. [[CrossRef](#)]
2. Maruyama, S.; Ikoma, M.; Genda, H.; Hirose, K.; Yokoyama, T.; Santosh, M. The naked planet Earth: Most essential pre-requisite for the origin and evolution of life. *Geosci. Front.* **2013**, *4*, 141–165. [[CrossRef](#)]
3. Zhu, R.; Hou, Z.; Guo, Z.; Wan, B. Summary of “the past, present and future of the habitable Earth: Development strategy of Earth science”. *Chin. Sci. Bull.* **2021**, *66*, 4485–4490. [[CrossRef](#)]
4. Wu, L.; Jing, Z.; Chen, X.; Li, C.; Zhang, G.; Wang, S.; Dong, B.; Zhuang, G. Marine science in China: Current status and future outlooks. *Earth Sci. Front.* **2022**, *29*, 1–12.
5. Niu, Y. Lithosphere thickness controls the extent of mantle melting, depth of melt extraction and basalt compositions in all tectonic settings on Earth—A review and new perspectives. *Earth-Sci. Rev.* **2021**, *217*, 103614. [[CrossRef](#)]
6. Gao, X.; Li, J.C.; Yuan, G.L.; Wang, G.H.; Liang, X.; Zheng, Y.L.; Wang, Q. Middle-Late Triassic magmatic records for the accretionary processes of South Qiangtang accretionary terrane: The mafic dykes in Mayigangri-Jiaomuri area North Tibet. *Acta Petrol. Sin.* **2019**, *35*, 760–774. [[CrossRef](#)]
7. Safonova, I.; Maruyama, S.; Kojima, S.; Komiya, T.; Krivonogov, S.; Koshida, K. Recognizing OIB and MORB in accretionary complexes: A new approach based on ocean plate stratigraphy, petrology and geochemistry. *Gondwana Res.* **2016**, *33*, 92–114. [[CrossRef](#)]
8. Pullen, A.; Kapp, P.; Gehrels, G.E.; Ding, L.; Zhang, Q. Metamorphic rocks in central Tibet: Lateral variations and implications for crustal structure. *Geol. Soc. Am. Bull.* **2011**, *123*, 585–600. [[CrossRef](#)]
9. Pullen, A.; Kapp, P.; Gehrels, G.E.; Vervoort, J.D.; Ding, L. Triassic continental subduction in central Tibet and Mediterranean-style closure of the Paleo-Tethys Ocean. *Geology* **2008**, *36*, 351–354. [[CrossRef](#)]
10. Kapp, P.; Yin, A.; Manning, C.E.; Harrison, T.M.; Taylor, M.H.; Ding, L. Tectonic evolution of the early Mesozoic blueschist-bearing Qiangtang metamorphic belt, central Tibet. *Tectonics* **2003**, *22*, 1043. [[CrossRef](#)]
11. Zhang, K.-J.; Zhang, Y.-X.; Li, B.; Zhu, Y.-T.; Wei, R.-Z. The blueschist-bearing Qiangtang metamorphic belt (northern Tibet, China) as an in situ suture zone: Evidence from geochemical comparison with the Jinsa suture. *Geology* **2006**, *34*, 493–496. [[CrossRef](#)]
12. Zhao, Z.; Bons, P.D.; Wang, G.; Soesoo, A.; Liu, Y. Tectonic evolution and high-pressure rock exhumation in the Qiangtang terrane, central Tibet. *Solid Earth* **2015**, *6*, 457–473. [[CrossRef](#)]
13. Li, D.; Wang, G.H.; Bons, P.D.; Zhao, Z.B.; Du, J.X.; Wang, S.L.; Yuan, G.L.; Liang, X.; Zhang, L.; Li, C.; et al. Subduction Reversal in a Divergent Double Subduction Zone Drives the Exhumation of Southern Qiangtang Blueschist-Bearing Mélange, Central Tibet. *Tectonics* **2019**, *39*, e2019TC006051. [[CrossRef](#)]
14. Li, C. Twenty years of research on the Longmucu-Shuanghu-Lancangjiang suture zone in the Qinghai-Tibetan Plateau. *Geol. Rev.* **2008**, *54*, 105–119.
15. Zhai, Q.-G.; Jahn, B.-M.; Zhang, R.-Y.; Wang, J.; Su, L. Triassic Subduction of the Paleo-Tethys in northern Tibet, China: Evidence from the geochemical and isotopic characteristics of eclogites and blueschists of the Qiangtang Block. *J. Asian Earth Sci.* **2011**, *42*, 1356–1370. [[CrossRef](#)]
16. Zhai, Q.G.; Zhang, R.Y.; Jahn, B.M.; Li, C.; Song, S.G.; Wang, J. Triassic eclogites from central Qiangtang, northern Tibet, China: Petrology, geochronology and metamorphic PT path. *Lithos* **2011**, *125*, 173–189. [[CrossRef](#)]
17. Zhang, X.-Z.; Dong, Y.-S.; Li, C.; Deng, M.-R.; Zhang, L.; Xu, W. Silurian high-pressure granulites from Central Qiangtang, Tibet: Constraints on early Paleozoic collision along the northeastern margin of Gondwana. *Earth Planet. Sci. Lett.* **2014**, *405*, 39–51. [[CrossRef](#)]
18. Zhang, X.-Z.; Dong, Y.-S.; Wang, Q.; Dan, W.; Zhang, C.; Deng, M.-R.; Xu, W.; Xia, X.-P.; Zeng, J.-P.; Liang, H. Carboniferous and Permian evolutionary records for the Paleo-Tethys Ocean constrained by newly discovered Xiangtaohu ophiolites from central Qiangtang, central Tibet. *Tectonics* **2016**, *35*, 1670–1686. [[CrossRef](#)]
19. Liang, X.; Wang, G.; Yang, B.; Ran, H.; Zheng, Y.; Du, J.; Li, L. Stepwise exhumation of the Triassic Lanling high-pressure metamorphic belt in Central Qiangtang, Tibet: Insights from a coupled study of metamorphism, deformation, and geochronology. *Tectonics* **2017**, *36*, 652–670. [[CrossRef](#)]
20. Xu, W.; Liu, F.; Dong, Y. Cambrian to Triassic geodynamic evolution of central Qiangtang, Tibet. *Earth-Sci. Rev.* **2020**, *201*, 103083. [[CrossRef](#)]
21. Fan, J.-J.; Li, C.; Xie, C.-M.; Liu, Y.-M.; Xu, J.-X.; Chen, J.-W. Remnants of late Permian–Middle Triassic ocean islands in northern Tibet: Implications for the late-stage evolution of the Paleo-Tethys Ocean. *Gondwana Res.* **2017**, *44*, 7–21. [[CrossRef](#)]

22. Liu, D.; Shi, R.; Ding, L.; Jiang, S.-Y. Survived Seamount Reveals an in situ Origin for the Central Qiangtang Metamorphic Belt in the Tibetan Plateau. *J. Earth Sci.* **2019**, *30*, 1253–1265. [[CrossRef](#)]
23. Kapp, P.; DeCelles, P.G. Mesozoic–Cenozoic geological evolution of the Himalayan–Tibetan orogen and working tectonic hypotheses. *Am. J. Sci.* **2019**, *319*, 159–254. [[CrossRef](#)]
24. Zhai, Q.-G.; Jahn, B.-M.; Li, X.-H.; Zhang, R.-Y.; Li, Q.-L.; Yang, Y.-N.; Wang, J.; Liu, T.; Hu, P.-Y.; Tang, S.-H. Zircon U–Pb dating of eclogite from the Qiangtang terrane, north-central Tibet: A case of metamorphic zircon with magmatic geochemical features. *Int. J. Earth Sci.* **2016**, *106*, 1239–1255. [[CrossRef](#)]
25. Zhang, X.Z.; Dong, Y.S.; Wang, Q.; Dan, W. High pressure metamorphic belt in central Qiangtang, Tibetan Plateau: Progress and unsolved problems. *Geol. Bull. China* **2018**, *37*, 1406–1416.
26. Dan, W.; Wang, Q.; White, W.M.; Zhang, X.-Z.; Tang, G.-J.; Jiang, Z.-Q.; Hao, L.-L.; Ou, Q. Rapid formation of eclogites during a nearly closed ocean: Revisiting the Pianshishan eclogite in Qiangtang, central Tibetan Plateau. *Chem. Geol.* **2018**, *477*, 112–122. [[CrossRef](#)]
27. Deng, X.; Ding, L.; Liu, X.; Yin, A.; Kapp, P.A.; Murphy, M.A.; Manning, C.E. Geochemical characteristics of the blueschists and its tectonic significance in the central Qiangtang area, Tibet. *Acta Petrol. Sin.* **2002**, *18*, 517–525.
28. Zhang, X.; Dong, Y.; Li, C.; Shi, J.; Wang, S. Geochemistry and tectonic significance of eclogites in central Qiangtang, Tibetan Plateau. *Geol. Bull. China* **2010**, *29*, 1804–1814.
29. Zhang, X.; Dong, Y.; Li, C.; Xie, C.; Wang, M.; Deng, M.; Zhang, L. A record of complex histories from oceanic lithosphere subduction to continental subduction and collision: Constraints on geochemistry of eclogite and blueschist in Central Qiangtang, Tibetan Plateau. *Acta Petrol. Sin.* **2014**, *30*, 2821–2834.
30. Zhai, Q.-G.; Jahn, B.-M.; Wang, J.; Su, L.; Mo, X.-X.; Wang, K.-L.; Tang, S.-H.; Lee, H.-Y. The Carboniferous ophiolite in the middle of the Qiangtang terrane, Northern Tibet: SHRIMP U–Pb dating, geochemical and Sr–Nd–Hf isotopic characteristics. *Lithos* **2013**, *168–169*, 186–199. [[CrossRef](#)]
31. Zhai, Q.-g.; Jahn, B.-m.; Wang, J.; Hu, P.-y.; Chung, S.-l.; Lee, H.-y.; Tang, S.-h.; Tang, Y. Oldest Paleo-Tethyan ophiolitic mélange in the Tibetan Plateau. *Geol. Soc. Am. Bull.* **2015**, *128*, 355–373. [[CrossRef](#)]
32. Wu, Y.-W.; Li, C.; Xu, M.-J.; Xie, C.-M.; Wang, M.; Xiong, S.-Q.; Fan, Z.-G. Petrology, geochemistry, and geochronology of mafic rocks from the Taoxinghu Devonian ophiolite, LongmuCo–Shuanghu–Lancang suture zone, northern Tibet: Evidence for an intra-oceanic arc–basin system. *Int. Geol. Rev.* **2016**, *58*, 441–454. [[CrossRef](#)]
33. Li, D.; Wang, G.-H.; Gao, J.; Yuan, G.; Zhou, J.; Fang, D.; Zhang, L.; Gong, Y.; Zhao, H. The continental subduction in the evolution of central qiangtang mélange belt and its tectonic significance. *Int. Geol. Rev.* **2018**, *61*, 1143–1170. [[CrossRef](#)]
34. Liang, X.; Wang, G.; Yuan, G.; Liu, Y. Structural sequence and geochronology of the Qomo Ri accretionary complex, Central Qiangtang, Tibet: Implications for the Late Triassic subduction of the Paleo-Tethys Ocean. *Gondwana Res.* **2012**, *22*, 470–481. [[CrossRef](#)]
35. Wang, G.; Li, D.; Liang, X.; Tang, Y. Determination of the double-layer structure in orogenic belts and its geological significance. *J. Geomech.* **2022**, *28*, 705–727.
36. Lou, H.; Dong, Y.; Zhang, X.; Deng, M.; Zhang, L.; Xu, W. Disintegration of Early Devonian Maoershan Formation and delineation of ophiolite mélange in Xiangtaohu area of central Qiangtang, south Tibet. *Geol. Bull. China* **2014**, *33*, 1391–1399.
37. Deng, M.; Dong, Y.; Zhang, X.; Zhang, L.; Xu, W.; Liu, J. Geochemical characteristics and tectonic implications of Hongjishan ophiolite in central and western part of Qiangtang, northern Tibetan Plateau. *Geol. Bull. China* **2014**, *33*, 1740–1749.
38. Peng, Z.; Geng, Q.; Pan, G.; Wang, L.; Zhang, Z.; Cong, F.; Guan, J. Zircon SHRIMP geochronology and Nd–Pb isotopic characteristics of the meta-basalt in the central part of Tibetan Plateau’s Qiangtang region. *Sci. China Earth Sci.* **2014**, *57*, 428–438. [[CrossRef](#)]
39. Black, L.P.; Kamo, S.L.; Allen, C.M.; Aleinikoff, J.N.; Davis, D.W.; Korsch, R.J.; Foudoulis, C. TEMORA 1: A new zircon standard for Phanerozoic U–Pb geochronology. *Chem. Geol.* **2003**, *200*, 155–170. [[CrossRef](#)]
40. Wiedenbeck, M.; Allé, P.; Corfu, F.; Griffin, W.L.; Meier, M.; Oberli, F.; Quadt, A.V.; Roddick, J.C.; Spiegel, W. Three Natural Zircon Standards for U–Th–Pb, Lu–Hf, Trace Element and Re Analyses. *Geostand. Geoanal. Res.* **1995**, *19*, 1–23. [[CrossRef](#)]
41. Sláma, J.; Košler, J.; Condon, D.J.; Crowley, J.L.; Gerdes, A.; Hanchar, J.M.; Horstwood, M.S.A.; Morris, G.A.; Nasdala, L.; Norberg, N.; et al. Plešovice zircon—A new natural reference material for U–Pb and Hf isotopic microanalysis. *Chem. Geol.* **2008**, *249*, 1–35. [[CrossRef](#)]
42. Liu, Y.; Gao, S.; Hu, Z.; Gao, C.; Zong, K.; Wang, D. Continental and Oceanic Crust Recycling-induced Melt–Peridotite Interactions in the Trans-North China Orogen: U–Pb Dating, Hf Isotopes and Trace Elements in Zircons from Mantle Xenoliths. *J. Petrol.* **2010**, *51*, 537–571. [[CrossRef](#)]
43. Ludwig, K.R. *ISOPLOT 3.0: A Geochronological Toolkit for Microsoft Excel*; Berkeley Geochronology Center Special Publication: Berkeley, CA, USA, 2003; Volume 39, pp. 91–445.
44. Andersen, T. Correction of common lead in U–Pb analyses that do not report ²⁰⁴Pb. *Chem. Geol.* **2002**, *192*, 59–79. [[CrossRef](#)]
45. Sun, P.; Niu, Y.; Guo, P.; Chen, S.; Duan, M.; Gong, H.; Wang, X.; Xiao, Y. Multiple mantle metasomatism beneath the Leizhou Peninsula, South China: Evidence from elemental and Sr–Nd–Pb–Hf isotope geochemistry of the late Cenozoic volcanic rocks. *Int. Geol. Rev.* **2018**, *61*, 1768–1785. [[CrossRef](#)]
46. Hoskin, P.; Black, L. Metamorphic zircon formation by solid-state recrystallization of protolith igneous zircon. *J. Metamorph. Geol.* **2000**, *18*, 423–439. [[CrossRef](#)]

47. Escuder-Viruete, J.; Pérez-Estaún, A.; Weis, D.; Friedman, R. Geochemical characteristics of the Río Verde Complex, Central Hispaniola: Implications for the paleotectonic reconstruction of the Lower Cretaceous Caribbean island-arc. *Lithos* **2010**, *114*, 168–185. [[CrossRef](#)]
48. Winchester, J.A.; Floyd, P.A. Geochemical discrimination of different magma series and their differentiation products using immobile elements. *Chem. Geol.* **1977**, *20*, 325–343. [[CrossRef](#)]
49. Pearce, J. Role of the sub-continental lithosphere in magma genesis at active continental margin. In *Continental Basalts and Mantle Xenoliths*; Hawkesworth, C.J., Norry, M.J., Eds.; Shiva Publications: Nantwich, UK, 1983; pp. 230–249.
50. Komiya, T.; Maruyama, S.; Hirata, T.; Yurimoto, H. Petrology and Geochemistry of MORB and OIB in the Mid-Archean North Pole Region, Pilbara Craton, Western Australia: Implications for the Composition and Temperature of the Upper Mantle at 3.5 Ga. *Int. Geol. Rev.* **2002**, *44*, 988–1016. [[CrossRef](#)]
51. Sun, S.-S.; McDonough, W.F. Chemical and isotopic systematics of oceanic basalts: Implications for mantle composition and processes. *Geol. Soc. Lond. Spec. Publ.* **1989**, *42*, 313–345. [[CrossRef](#)]
52. Pearce, J.A.; Cann, J.R. Tectonic setting of basic volcanic rocks determined using trace element analyses. *Earth Planet. Sci. Lett.* **1973**, *19*, 290–300. [[CrossRef](#)]
53. Li, S. Ba-Nb-Th-La Diagrams Used to Identify Tectonic Environments of Ophiolite. *Acta Petrol. Sin.* **1993**, *9*, 146–157.
54. Murray, R.W. Chemical criteria to identify the depositional environment of chert: General principles and applications. *Sediment. Geol.* **1994**, *90*, 213–232. [[CrossRef](#)]
55. Haskin, L.A.; Haskin, M.A.; Frey, F.A.; Wildeman, T.R. Relative and Absolute Terrestrial Abundances of the Rare Earths. In *Origin and Distribution of the Elements*; Ahrens, L.H., Ed.; Pergamon: Oxford, UK, 1968; pp. 889–912.
56. Verma, S.P. Seawater alteration effects on ⁸⁷Sr/⁸⁶Sr, K, Rb, Cs, Ba and Sr in oceanic igneous rocks. *Chem. Geol.* **1981**, *34*, 81–89. [[CrossRef](#)]
57. Xu, J.-F.; Castillo, P.R. Geochemical and Nd–Pb isotopic characteristics of the Tethyan asthenosphere: Implications for the origin of the Indian Ocean mantle domain. *Tectonophysics* **2004**, *393*, 9–27. [[CrossRef](#)]
58. Liu, H.; Chen, Y.; Shang, Z. Zircon U–Pb Geochronology, Geochemistry and Geological Significance of the Santaishan–Yingjiang Ultramafic Rocks in Western Yunnan, China. *Minerals* **2023**, *13*, 536. [[CrossRef](#)]
59. Porter, K.A.; White, W.M. Deep mantle subduction flux. *Geochem. Geophys. Geosyst.* **2009**, *10*, Q12016. [[CrossRef](#)]
60. Bea, F.; Fershtater, G.B.; Montero, P.; Whitehouse, M.; Levin, V.Y.; Scarrow, J.H.; Austrheim, H.; Pushkariev, E.V. Recycling of continental crust into the mantle as revealed by Kytlym dunite zircons, Ural Mts, Russia. *Terra Nova* **2001**, *13*, 407–412. [[CrossRef](#)]
61. Bea, F.; Montero, P.; Palma, J.F.M. Experimental evidence for the preservation of U–Pb isotope ratios in mantle-recycled crustal zircon grains. *Sci. Rep.* **2018**, *8*, 12904. [[CrossRef](#)]
62. Skolotnev, S.G.; Bel'tenev, V.E.; Lepekina, E.N.; Ipat'eva, I.S. Younger and older zircons from rocks of the oceanic lithosphere in the Central Atlantic and their geotectonic implications. *Geotectonics* **2010**, *44*, 462–492. [[CrossRef](#)]
63. Torsvik, T.H.; Amundsen, H.; Hartz, E.H.; Corfu, F.; Kuznir, N.; Gaina, C.; Doubrovine, P.V.; Steinberger, B.; Ashwal, L.D.; Jamtveit, B. A Precambrian microcontinent in the Indian Ocean. *Nat. Geosci.* **2013**, *6*, 223–227. [[CrossRef](#)]
64. Bea, F.; Bortnikov, N.; Montero, P.; Zinger, T.; Sharkov, E.; Silant'ev, S.; Skolotnev, S.; Trukhalev, A.; Molina-Palma, J.F. Zircon xenocryst evidence for crustal recycling at the Mid-Atlantic Ridge. *Lithos* **2020**, *354–355*, 105361. [[CrossRef](#)]
65. Condie, K.C. Chemical composition and evolution of the upper continental crust: Contrasting results from surface samples and shales. *Chem. Geol.* **1993**, *104*, 1–37. [[CrossRef](#)]
66. Neal, C.R.; Mahoney, J.J.; Chazey, W.J., III. Mantle Sources and the Highly Variable Role of Continental Lithosphere in Basalt Petrogenesis of the Kerguelen Plateau and Broken Ridge LIP: Results from ODP Leg 183. *J. Petrol.* **2002**, *43*, 1177–1205. [[CrossRef](#)]
67. Rudnick, R.L.; Gao, S. 3.01—Composition of the Continental Crust. In *Treatise on Geochemistry*; Holland, H.D., Turekian, K.K., Eds.; Pergamon: Oxford, UK, 2003; pp. 1–64.
68. La Flèche, M.R.; Camiré, G.; Jenner, G.A. Geochemistry of post-Acadian, Carboniferous continental intraplate basalts from the Maritimes Basin, Magdalen Islands, Québec, Canada. *Chem. Geol.* **1998**, *148*, 115–136. [[CrossRef](#)]
69. McCulloch, M.T.; Bennett, V.C. Progressive growth of the Earth's continental crust and depleted mantle: Geochemical constraints. *Geochim. Cosmochim. Acta* **1994**, *58*, 4717–4738. [[CrossRef](#)]
70. Niu, Y. Some basic concepts and problems on the petrogenesis of intra-plate ocean island basalts. *Chin. Sci. Bull.* **2009**, *54*, 4148–4160. [[CrossRef](#)]
71. Reagan, M.K.; Gill, J.B. Coexisting calcalkaline and high-niobium basalts from Turrialba Volcano, Costa Rica: Implications for residual titanates in arc magma sources. *J. Geophys. Res. Solid Earth* **1989**, *94*, 4619–4633. [[CrossRef](#)]
72. Xu, Y.; Chung, S.-L.; Jahn, B.-M.; Wu, G. Petrologic and geochemical constraints on the petrogenesis of Permian–Triassic Emeishan flood basalts in southwestern China. *Lithos* **2001**, *58*, 145–168. [[CrossRef](#)]
73. Haase, K.M.; Stoffers, P.; Garbe-Schönberg, C.D. The Petrogenetic Evolution of Lavas from Easter Island and Neighbouring Seamounts, Near-ridge Hotspot Volcanoes in the SE Pacific. *J. Petrol.* **1997**, *38*, 785–813. [[CrossRef](#)]
74. Haase, K.M.; Beier, C.; Kemner, F. A Comparison of the Magmatic Evolution of Pacific Intraplate Volcanoes: Constraints on Melting in Mantle Plumes. *Front. Earth Sci.* **2019**, *6*, 242. [[CrossRef](#)]
75. Whitaker, M.L.; Nekvasil, H.; Lindsley, D.H.; Difrancesco, N.J. The Role of Pressure in Producing Compositional Diversity in Intraplate Basaltic Magmas. *J. Petrol.* **2007**, *48*, 365–393. [[CrossRef](#)]

76. Niu, Y.; Wilson, M.; Humphreys, E.R.; O'hara, M.J. The origin of intra-plate ocean island basalts (OIB): The lid effect and its geodynamic implications. *J. Petrol.* **2011**, *52*, 1443–1468. [[CrossRef](#)]
77. McKenzie, D.A.N.; O'Nions, R.K. Partial Melt Distributions from Inversion of Rare Earth Element Concentrations. *J. Petrol.* **1991**, *32*, 1021–1091. [[CrossRef](#)]
78. Horn, I.; Foley, S.F.; Jackson, S.E.; Jenner, G.A. Experimentally determined partitioning of high field strength- and selected transition elements between spinel and basaltic melt. *Chem. Geol.* **1994**, *117*, 193–218. [[CrossRef](#)]
79. Hart, S.R.; Dunn, T. Experimental cpx/melt partitioning of 24 trace elements. *Contrib. Mineral. Petrol.* **1993**, *113*, 1–8. [[CrossRef](#)]
80. Hauri, E.H.; Wagner, T.P.; Grove, T.L. Experimental and natural partitioning of Th, U, Pb and other trace elements between garnet, clinopyroxene and basaltic melts. *Chem. Geol.* **1994**, *117*, 149–166. [[CrossRef](#)]
81. Aldanmaz, E.; Pearce, J.A.; Thirlwall, M.F.; Mitchell, J.G. Petrogenetic evolution of late Cenozoic, post-collision volcanism in western Anatolia, Turkey. *J. Volcanol. Geotherm. Res.* **2000**, *102*, 67–95. [[CrossRef](#)]
82. McKenzie, D.A.N.; O'Nions, R.K. The Source Regions of Ocean Island Basalts. *J. Petrol.* **1995**, *36*, 133–159. [[CrossRef](#)]
83. Fitton, J.G.; Saunders, A.D.; Norry, M.J.; Hardarson, B.S.; Taylor, R.N. Thermal and chemical structure of the Iceland plume. *Earth Planet. Sci. Lett.* **1997**, *153*, 197–208. [[CrossRef](#)]
84. Frey, F.A.; Green, D.H.; Roy, S.D. Integrated Models of Basalt Petrogenesis: A Study of Quartz Tholeiites to Olivine Melilitites from South Eastern Australia Utilizing Geochemical and Experimental Petrological Data. *J. Petrol.* **1978**, *19*, 463–513. [[CrossRef](#)]
85. Hess, P.C. Phase equilibria constraints on the origin of ocean floor basalts. *Wash. DC Am. Geophys. Union Geophys. Monogr. Ser.* **1992**, *71*, 67–102. [[CrossRef](#)]
86. Wilson, M. *Igneous Petrogenesis: A Global Tectonic Approach*; Unwin Hyman: London, UK, 1989.
87. Jung, S.; Masberg, P. Major- and trace-element systematics and isotope geochemistry of Cenozoic mafic volcanic rocks from the Vogelsberg (central Germany). *J. Volcanol. Geotherm. Res.* **1998**, *86*, 151–177. [[CrossRef](#)]
88. Humphreys, E.R.; Niu, Y. On the composition of ocean island basalts (OIB): The effects of lithospheric thickness variation and mantle metasomatism. *Lithos* **2009**, *112*, 118–136. [[CrossRef](#)]
89. Kato, Y. Origin and global tectonic significance of Early Archean cherts from the Marble Bar greenstone belt, Pilbara Craton, Western Australia. *Precambrian Res.* **2003**, *125*, 191–243. [[CrossRef](#)]
90. Murray, R.W.; Buchholtz ten Brink, M.R.; Jones, D.L.; Gerlach, D.C.; Russ, G.P., III. Rare earth elements as indicators of different marine depositional environments in chert and shale. *Geology* **1990**, *18*, 268–271. [[CrossRef](#)]
91. Girty, G.H.; Ridge, D.L.; Knaack, C.; Johnson, D.; Al-Riyami, R.K. Provenance and depositional setting of Paleozoic chert and argillite, Sierra Nevada, California. *J. Sediment. Res.* **1996**, *66*, 107–118. [[CrossRef](#)]
92. Malovitskiy, Y.P.; Emelyanov, E.M.; Kazakov, O.V.; Moskalenko, V.N.; Osipov, G.V.; Shimkus, K.M.; Chumakov, I.S. Geological structure of the Mediterranean Sea floor (based on geological—Geophysical data). *Mar. Geol.* **1975**, *18*, 231–261. [[CrossRef](#)]
93. Dan, W.; Wang, Q.; White, W.M.; Li, X.-H.; Zhang, X.-Z.; Tang, G.-J.; Ou, Q.; Hao, L.-L.; Qi, Y. Passive-margin magmatism caused by enhanced slab-pull forces in central Tibet. *Geology* **2020**, *49*, 130–134. [[CrossRef](#)]
94. Yang, T.N.; Zhang, H.R.; Liu, Y.X.; Wang, Z.L.; Song, Y.C.; Yang, Z.S.; Tian, S.H.; Xie, H.Q.; Hou, K.J. Permo-Triassic arc magmatism in central Tibet: Evidence from zircon U–Pb geochronology, Hf isotopes, rare earth elements, and bulk geochemistry. *Chem. Geol.* **2011**, *284*, 270–282. [[CrossRef](#)]
95. Peng, T.; Zhao, G.; Fan, W.; Peng, B.; Mao, Y. Late Triassic granitic magmatism in the Eastern Qiangtang, Eastern Tibetan Plateau: Geochronology, petrogenesis and implications for the tectonic evolution of the Paleo-Tethys. *Gondwana Res.* **2015**, *27*, 1494–1508. [[CrossRef](#)]
96. Zhang, K.-J.; Tang, X.-C.; Wang, Y.; Zhang, Y.-X. Geochronology, geochemistry, and Nd isotopes of early Mesozoic bimodal volcanism in northern Tibet, western China: Constraints on the exhumation of the central Qiangtang metamorphic belt. *Lithos* **2011**, *121*, 167–175. [[CrossRef](#)]
97. Lu, L.; Qin, Y.; Li, Z.-F.; Yan, L.-L.; Jin, X.; Zhang, K.-J. Diachronous closure of the Shuanghu Paleo-Tethys Ocean: Constraints from the Late Triassic Tanggula arc-related volcanism in the East Qiangtang subterranean, Central Tibet. *Lithos* **2019**, *328*, 182–199. [[CrossRef](#)]
98. Fan, J.-J.; Li, C.; Xie, C.-M.; Liu, Y.-M. Depositional environment and provenance of the upper Permian–Lower Triassic Tianquan-shan Formation, northern Tibet: Implications for the Palaeozoic evolution of the Southern Qiangtang, Lhasa, and Himalayan terranes in the Tibetan Plateau. *Int. Geol. Rev.* **2016**, *58*, 228–245. [[CrossRef](#)]
99. Li, C.; Zhai, Q.; Dong, Y.; Yu, J.; Huang, X. Establishment of the Unner Triassic Wanchulinn Formation at Guoganjianian Mountain, central Qiangtang, Qinghai-Tibet Plateau, and its significance. *Geol. Bull. China* **2007**, *26*, 1003–1008.
100. Jin, X.; Zhang, Y.-X.; Zhou, X.-Y.; Zhang, K.-J.; Li, Z.-W.; Khalid, S.B.; Hu, J.-C.; Lu, L.; Sun, W.-D. Protoliths and tectonic implications of the newly discovered Triassic Baqing eclogites, central Tibet: Evidence from geochemistry, Sr Nd isotopes and geochronology. *Gondwana Res.* **2019**, *69*, 144–162. [[CrossRef](#)]
101. Wu, Y.; Li, C.; Xie, C.; Wang, M.; Hu, P. Petrology and geochronology of Guoganjianianshan Permian ophiolite in central Qiangtang, Qinghai-Tibet Plateau, China. *Geol. Bull. China* **2010**, *29*, 1773–1780.
102. Chen, Y.; Ye, K. Exhumation of subducted oceanic crust: Key issues and discussion. *Acta Petrol. Sin.* **2013**, *29*, 1461–1478.
103. Tian, Y.; Liang, X.; Wang, G.; Tang, Y.; Chen, S.; Gao, X.; Yang, B.; Guo, Z.; Wang, Y.; Wen, J. Protolith origin of the Lanling high-pressure metamorphic terrane in central Qiangtang, Tibet, reveals the subduction of the Permian–Triassic ocean island and abyssal submarine fan in the Paleo-Tethys Ocean. *Gondwana Res.* **2023**, *121*, 404–417. [[CrossRef](#)]

104. Ou, Q.; Wang, Q.; Zeng, J.-P.; Yang, J.-H.; Zhang, H.-X.; Xia, X.-P.; Chen, Y.-W. Petrogenesis and tectonic implications of Middle Triassic basalts and rhyolites in the northern Qiangtang Block, central Tibet. *J. Asian Earth Sci.* **2021**, *206*, 104573. [[CrossRef](#)]
105. He, H.; Li, Y.; Wang, T.; Xiao, S.; Wang, Z.; Chen, L.; Feng, Z.; Han, S.; Liu, S.; Zhang, Y.; et al. Late Triassic granites (ca. 230 Ma) from Cairi area in eastern Qiangtang subterrane, central Tibet: Product of a mid-oceanic ridge subduction. *Geol. J.* **2022**, *57*, 150–165. [[CrossRef](#)]
106. Wang, Q.; Wyman, D.A.; Xu, J.; Wan, Y.; Li, C.; Zi, F.; Jiang, Z.; Qiu, H.; Chu, Z.; Zhao, Z.; et al. Triassic Nb-enriched basalts, magnesian andesites, and adakites of the Qiangtang terrane (Central Tibet): Evidence for metasomatism by slab-derived melts in the mantle wedge. *Contrib. Mineral. Petrol.* **2007**, *155*, 473–490. [[CrossRef](#)]
107. Zhang, H.; Yang, T.; Hou, Z.; Wang, Y. Magmatic expression of tectonic transition from oceanic subduction to continental collision: Insights from the Middle Triassic rhyolites of the North Qiangtang Block. *Gondwana Res.* **2020**, *87*, 67–82. [[CrossRef](#)]
108. Wang, J.; Fu, X.; Wei, H.; Shen, L.; Wang, Z.; Li, K. Late Triassic basin inversion of the Qiangtang Basin in northern Tibet: Implications for the closure of the Paleo-Tethys and expansion of the Neo-Tethys. *J. Asian Earth Sci.* **2022**, *227*, 105119. [[CrossRef](#)]
109. Fu, X.; Wang, J.; Tan, F.; Chen, M.; Chen, W. The Late Triassic rift-related volcanic rocks from eastern Qiangtang, northern Tibet (China): Age and tectonic implications. *Gondwana Res.* **2010**, *17*, 135–144. [[CrossRef](#)]
110. Li, J.; Zhao, Z.; Zheng, Y.; Yuan, G.; Liang, X.; Wang, G.; Liu, X. The magmatite evidences in southern Qiangtang for paleo-Tethys ocean subducting collision: Gangtang-co granites in Rongma, Tibet. *Acta Petrol. Sin.* **2015**, *31*, 2078–2088.

Disclaimer/Publisher’s Note: The statements, opinions and data contained in all publications are solely those of the individual author(s) and contributor(s) and not of MDPI and/or the editor(s). MDPI and/or the editor(s) disclaim responsibility for any injury to people or property resulting from any ideas, methods, instructions or products referred to in the content.